Early Cretaceous to Cenozoic Growth of the Patagonian Andes as Revealed by Low-Temperature Thermochronology

Gonzalo Ronda, Matías C Ghiglione, Joseph Martinod, Vanesa Barberón, Miguel E Ramos, Isabelle Coutand, Djordje Grujic, Roman Kislitsyn

To cite this version:

Gonzalo Ronda, Matías C Ghiglione, Joseph Martinod, Vanesa Barberón, Miguel E Ramos, et al.. Early Cretaceous to Cenozoic Growth of the Patagonian Andes as Revealed by Low-Temperature Thermochronology. Tectonics, 2022, 41 (10), pp.e2021TC007113. ⟨10.1029/2021TC007113⟩. ⟨hal-04942257⟩

HAL Id: hal-04942257
https://hal.science/hal-04942257v1
Submitted on 12 Feb 2025

Tectonics

RESEARCH ARTICLE
10.1029/2021TC007113

Key Points:

- We applied low-temperature thermochronology and thermal modeling to study timing and drivers of cooling in the Patagonian Andes at the Chile triple junction
- A Cretaceous cooling phase between 120 and 80 Ma was detected, directly linked to the first recorded Andean orogenic phase of the Patagonian Andes
- A 30-10 Ma cooling phase is related to the main phase of crustal shortening during increased convergence prior to the collision of the Chile ridge; 7-0 Ma cooling is likely linked to glaciations rather than to the development of slab window

Supporting Information:

Supporting Information may be found in the online version of this article.

Correspondence to:

G. Ronda,
ronda@gl.fcen.uba.ar;
gonzaloronda@gmail.com

Citation:

Ronda, G., Ghiglione, M. C., Martinod, J., Barberón, V., Ramos, M. E., Coutand, I., et al. (2022). Early Cretaceous to Cenozoic growth of the Patagonian Andes as revealed by low-temperature thermochronology. *Tectonics*, *41*, e2021TC007113. https://doi.org/10.1029/2021TC007113

Received 18 OCT 2021
Accepted 16 AUG 2022

Author Contributions:

Conceptualization: Gonzalo Ronda, Matías C. Ghiglione, Isabelle Coutand
Data curation: Gonzalo Ronda, Joseph Martinod
Funding acquisition: Matías C. Ghiglione, Isabelle Coutand, Djordje Grujic
Investigation: Gonzalo Ronda, Joseph Martinod, Vanesa Barberón, Miguel E. Ramos, Isabelle Coutand
Methodology: Gonzalo Ronda, Vanesa Barberón, Miguel E. Ramos, Isabelle

Early Cretaceous to Cenozoic Growth of the Patagonian Andes as Revealed by Low-Temperature Thermochronology

Gonzalo Ronda[1], Matías C. Ghiglione[1], Joseph Martinod[2], Vanesa Barberón[1], Miguel E. Ramos[1], Isabelle Coutand[3], Djordje Grujic[3], and Roman Kislitsyn[3]

[1]Instituto de Estudios Andinos "Don Pablo Groeber", Universidad de Buenos Aires, CONICET, Buenos Aires, Argentina, [2]Université Savoie Mont Blanc, Chambery, France, [3]Department of Earth and Environmental Sciences, Dalhousie University, Halifax, NS, Canada

Abstract The Southern Patagonian Andes at the latitude of the Chile Triple junction in Argentina and Chile (46°–47.5°S) are the object of an ongoing discussion regarding their orogenic evolution in terms of tectonic crustal thickening and exhumation. Recent works point to an Early Cretaceous onset of shortening according to observations in foreland sequences. The ensuing Cenozoic thermal history of the region was influenced by increased shortening, oceanic-ridge collision and formation of asthenospheric windows in a dynamic subduction setting. Furthermore, the onset of Patagonian glaciations after 7 Ma added increased complexities to the analysis of the main drivers of crustal cooling in this region. We applied zircon (U-Th)/He and apatite fission track thermochronometry, and inverse thermal modeling to unravel the thermal history throughout different structural domains of the Patagonian Andes. New thermochronological data and thermal models showed a previously unrecognized set of Cretaceous cooling ages (120-80 Ma) toward the foreland, that we relate to the onset of contraction during initial tectonic inversion. Toward the hinterland, Cenozoic cooling ages predominate, and are related to Oligocene-Miocene contraction in response to increased subduction velocities. Based on the regional distribution of thermochronological ages and on results from thermal modeling, a resetting of the zircon (U-Th)/He and apatite fission track systems in response to crustal heating related to the formation of an asthenospheric window after 16 Ma appears unlikely. After 7 Ma cooling rates increased in response to enhanced glacial erosion.

Plain Language Summary In this work, we have used thermochronometers, basically clocks that start recording time once a rock-sample has crossed a given temperature in the crust, to track the cooling of rock-samples from the Patagonian Andes between 46.5°S and 48°S. In this area, several processes influenced the evolution of the landscape such as mountain building, glaciers erosion, and deep-seated processes within the mantle. All of them may have left a trace in thermochronometers. Our goal is to determine the role of mountain building processes in rock cooling in this area. Our results suggest that rocks cooled in response to mountain building during the Cretaceous in what could be considered the first phase of construction of the Andes in the area. Mountain building processes continued influencing rock cooling during the Miocene, nearly 100 million-years after the first phase. During the last 7 million-years before the present, the onset of glacial erosion enhanced rock cooling. Finally, we found no records that the rocks heated in response to deep-seated mantle processes.

1. Introduction

A complex interaction of endogenous and exogenous processes took place in the Southern Patagonian Andes (SPA) at the latitude of the Chile triple junction (CTJ) (Figure 1), resulting from Cretaceous-Miocene tectonic crustal shortening and thickening in a geodynamic setting involving the subduction of oceanic ridges and late Miocene-Quaternary glaciations (e.g., Ghiglione et al., 2016; Mercer & Sutter, 1982; Ramos, 1989; Ramos & Kay, 1992).

Initial Aptian-Cenomanian contractional deformation in the SPA was suggested by forced regressions in the foreland basin (Ghiglione et al., 2015) and angular unconformities separating Cretaceous from younger rocks (Aramendía et al., 2018; Ronda et al., 2019). However, the regional distribution of Cretaceous low-temperature thermochronometric ages is insufficient to backup a direct relation between cooling and shortening (Fernández et al., 2020; Fosdick et al., 2013). Within the studied area (Figure 1) existing Cretaceous zircon (U-Th)/He and

Coutand, Djordje Grujic, Roman Kislitsyn
Resources: Matías C. Ghiglione, Isabelle Coutand, Djordje Grujic
Supervision: Matías C. Ghiglione, Isabelle Coutand
Writing – original draft: Gonzalo Ronda
Writing – review & editing: Matías C. Ghiglione, Joseph Martinod, Isabelle Coutand, Djordje Grujic

zircon fission tracks data have been linked to cooling following crystallization (Andrić-Tomašević et al., 2021; Thomson et al., 2001).

According to thermochronological studies, Miocene surface uplift and rock exhumation in the SPA have likely been influenced by (a) tectonic (contractional deformation; Thomson et al., 2001, 2010; Haschke et al., 2006; Georgieva et al., 2016, 2019), (b) geodynamic (dynamic uplift; Guillaume et al., 2009, 2013; Stevens-Goddard & Fosdick, 2019), and (c) climatic (glacial) processes (Christeleit et al., 2017; Georgieva et al., 2016, 2019; Thomson et al., 2010; Willett et al., 2020), with little consensus on which one dominated late Cenozoic exhumation in the SPA.

Regarding tectonic processes (a), low-temperature thermochronological data including apatite and zircon fission track and (U-Th)/He data (AFT, ZFT, AHe, and ZHe, respectively), have been used to constrain the duration of a late Cenozoic crustal thickening phase in the SPA between 30 and 8 Ma (Andrić-Tomašević et al., 2021; Thomson et al., 2001).

One of the most important geodynamic processes that occurred in the region (b) was the collision of the Chile ridge during the past 18-14 Myr (Breitsprecher & Thorkelson, 2009; Cande & Leslie, 1986), that caused the development of the Patagonian asthenospheric window (PAW) (Figure 1). Its impact in the crust could have produced dynamic surface uplift and coeval exhumation in the retroarc and foreland (Dávila et al., 2018; Guillaume et al., 2009, 2013). It has been suggested that the thermal impact of the PAW has caused an estimated heating of the upper crust of 60 ± 30°C between 10 and 6 Ma according to AFT data modeling in Cerro Barrancos (Figure 2) (Haschke et al., 2006) and of 100°C between 15 and 10 Ma at 1.4–1.75 Km depth in the crust, due to changing mantle dynamics preceding the PAW (Guillaume et al., 2013). Ávila and Dávila (2018) also registered an increase in heat flow according to recent borehole data. These heating phases have been questioned by further modeling (Christeleit et al., 2017; Georgieva et al., 2019).

Important climatic changes (c) took place during the Miocene related to the onset of Patagonian glaciations (Mercer & Sutter, 1982). Post-Miocene increase in cooling and erosion-rates in the CTJ region have been attributed to glacial erosion during the past 7 Myr (Christeleit et al., 2017; Herman et al., 2013; Thomson et al., 2010; Willett et al., 2020) or to a combination of glacial erosion and transpression (Georgieva et al., 2016, 2019). It has also been suggested that focused glacial erosion promoted out-of-sequence thrusting in the hinterland and stagnation of the fold-and-thrust belt (FTB) (Ghiglione et al., 2019; Ronda et al., 2019; Thomson et al., 2010).

This work aims to investigate the impact that Cretaceous to Cenozoic crustal shortening had on the cooling of the SPA between 46.5° and 48°S. A new thermochronological data set was acquired, including 50 bedrock ZHe and 19 AFT ages broadly distributed along two structural transects across the orogen (Figures 1 and 2). New data were integrated with published datasets (Andrić-Tomašević et al., 2021; Christeleit et al., 2017; Georgieva et al., 2016; Guillaume et al., 2013; Haschke et al., 2006; Thomson et al., 2010) to constrain inverse thermal models and address the thermal history of the study area.

2. Geodynamic and Geologic Setting

2.1. Geodynamic Setting

The Pacific margin at the latitude of the study area is characterized by the ridge-trench-trench type CTJ which formed in the middle Miocene and migrated northwards to its present position (Figure 1; Cande & Leslie, 1986; Breitsprecher & Thorkelson, 2009). North of the CTJ, the Nazca plate (Figure 1) is subducting obliquely at 7.3 cm/yr toward the NE, while to the south, the Antarctic plate subducts at a slower 2 cm/yr toward the E (DeMets et al., 2010). The difference in convergence rates and directions between Nazca and Antarctic plates favored the opening of the PAW, beneath South America, during the past ∼16 Ma (Breitsprecher & Thorkelson, 2009) while the CTJ migrated northwards (Figure 1). During ridge collision arc volcanism decreased substantially (Ramos & Kay, 1992), whereas extensive Miocene back-arc plateau volcanism developed (Gorring et al., 1997; Guivel et al., 2006).

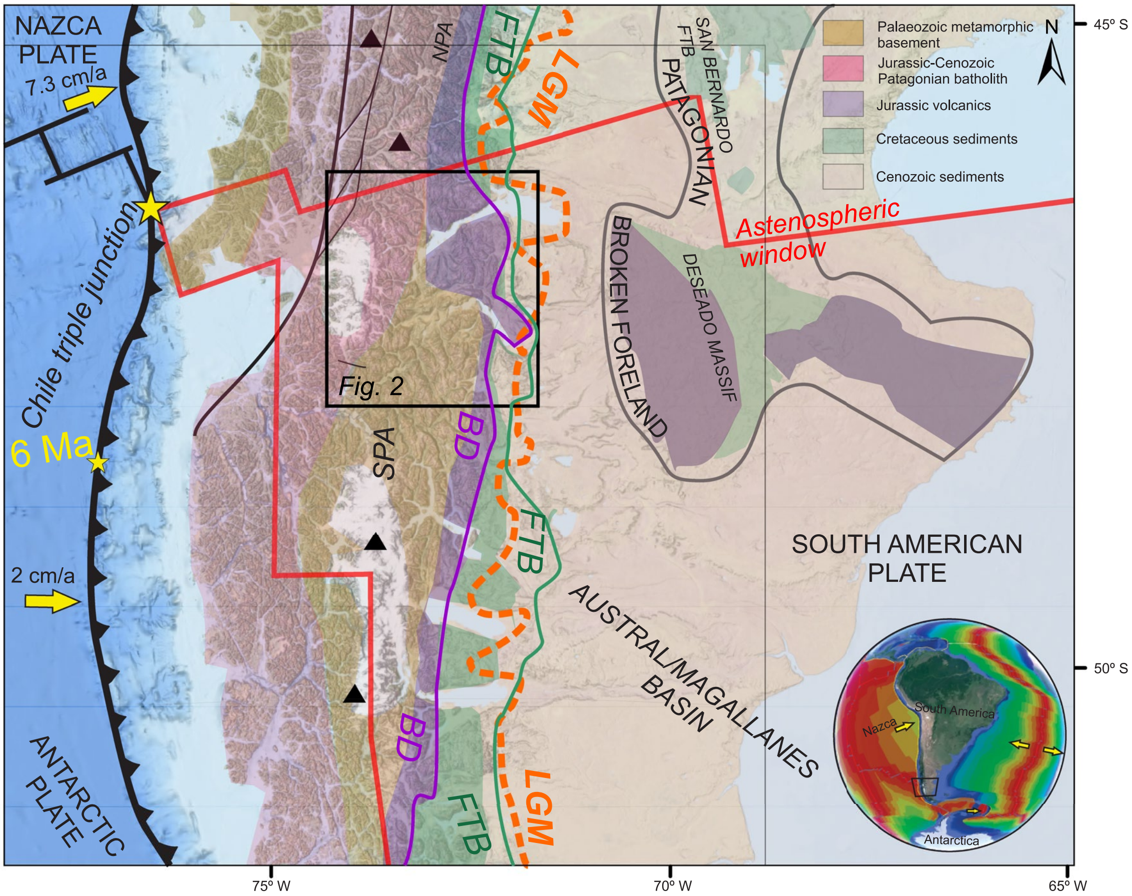

Figure 1. Geodynamic and geological setting of Patagonia. Nazca and Antarctic plates are subducting at different directions and velocities underneath South America (velocities are from MORVEL, DeMets et al., 2010). Yellow stars mark the present and past location of the CTJ, red lines mark the present boundaries of the asthenospheric window according to Breitsprecher and Thorkelson (2009). Black triangles are Holocene volcanoes from Ramos and Kay (1992). Orange line is the eastern extent of the Last Glacial Maximum according to Coronato et al. (2004) and Glasser et al. (2008). The black box indicates the location of the study area. SPA: Southern Patagonian Andes; NPA: North Patagonian Andes; FTB: fold-and-thrust belt; BD: basement domain including Paleozoic metamorphic and Jurassic volcanic rocks. Purple line: extent of the BD. Green line: extent of FTB.

2.2. Geologic Setting

The Paleozoic greenschist-facies metasedimentary basement of the study area was intruded by the Upper Jurassic to Cenozoic Southern Patagonian batholith (SPB) formed by calc-alkaline gabbroic to granitoid plutons (Figure 2; Rb-Sr in whole rock, Pankhurst et al., 1999; U-Pb on zircons, Hervé et al., 2007). During the Late Jurassic (150–142 Ma), the region experienced crustal extension, represented by El Quemado Complex synrift felsic volcanics (Figure 2; Pankhurst et al., 2000; Calderón et al., 2007), and the formation of oceanic crust in the Rocas Verdes back-arc basin (Calderón et al., 2007).

After an initial extensional event, during the Early Cretaceous, the Austral-Magallanes basin underwent thermal subsidence characterized by Berriasian to Barremian transgressive sedimentary sequences followed by initial foreland Aptian-Albian littoral and continental facies (Aramendía et al., 2018; Ghiglione et al., 2015). A Late Cretaceous-Paleocene regional depositional hiatus follows marked by the finding of folded and thrusted upper Cretaceous rocks that are covered by the unconformable Eocene Posadas basalt (Figure 2; Aramendía et al., 2018). These observations were interpreted as the result of Aptian-Cenomanian contractional deformation and basin inversion (Ronda et al., 2019). Nearby records of the onset of Cretaceous shortening were found in the San Bernardo FTB (Figure 1; Gianni et al., 2015) and the Deseado Massif (Figure 1) and are associated with a broken foreland stage and a proposed Cretaceous flat subduction in Patagonia between 121 and 80 Ma (Gianni et al., 2018). During the Eocene, the Farallon-Aluk ridge collided with southernmost South America (Cande & Leslie, 1986; Somoza & Ghidella, 2012) and generated widespread back-arc volcanism such as the Posadas,

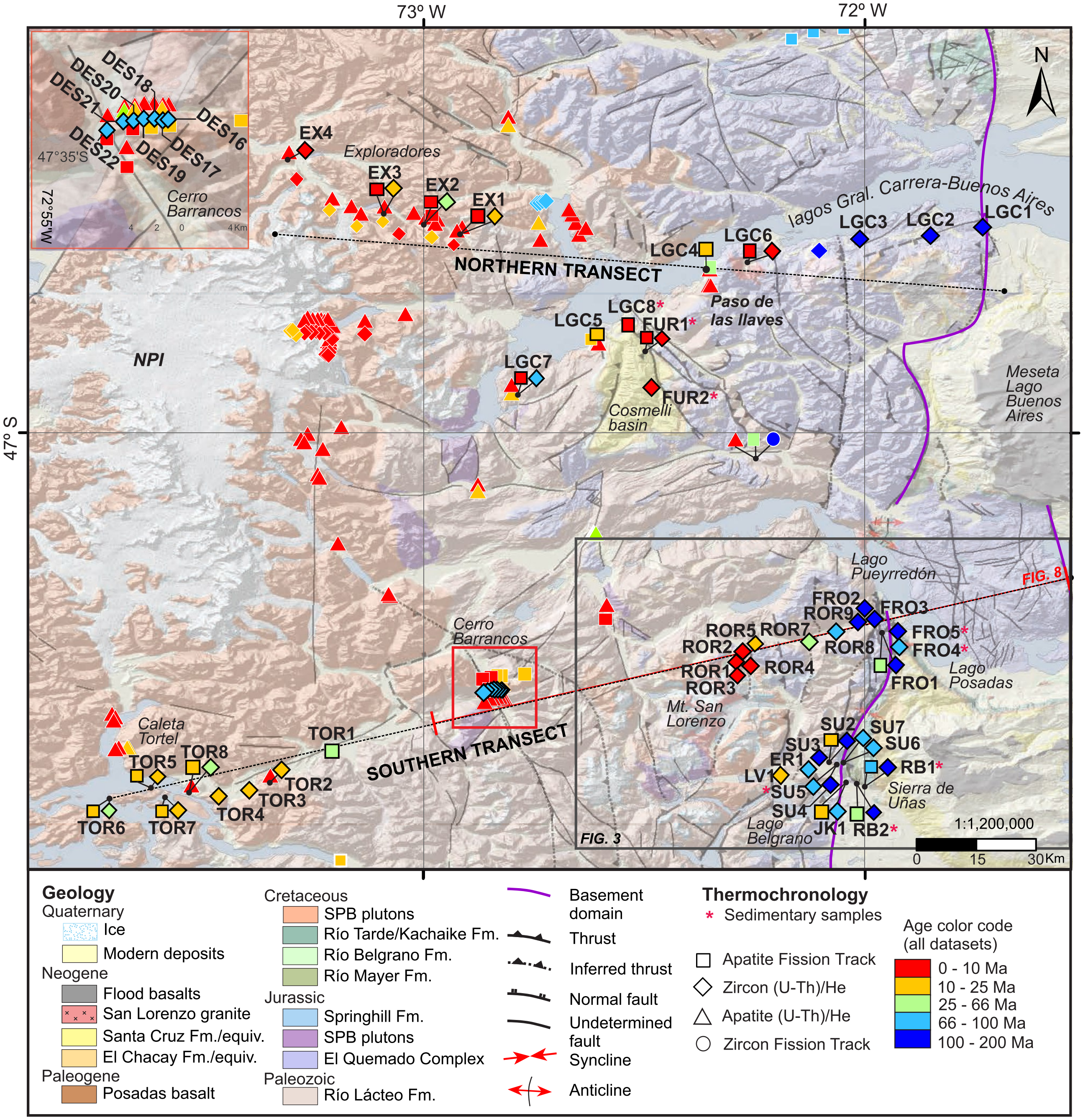

Figure 2. Geologic map of the study area (data are from Ramos, 1989; De la Cruz et al., 2004; Ronda et al., 2019) with locations of new and existing thermochronological samples. Samples with white contours are from previous datasets: Haschke et al., 2006; Thomson et al., 2001, 2010; Guillaume et al., 2013; Georgieva et al., 2016; Christeleit et al., 2017; Andrić-Tomašević et al., 2021. Samples with black contours and labels are new AFT and ZHe ages. Locations of study transects are indicated by the black lines. Red segment along the southern transect marks the extent of Figure 8.

Meseta Chile Chico and Balmaceda flood basalts constrained between 57–40 Ma, interpreted as a first evidence of an asthenospheric window underneath the area (Espinoza et al., 2005; Ramos & Kay, 1992).

The increase in convergence rate between Nazca and South America plates after ~28–25 Ma (Pardo-Casas & Molnar, 1987; Somoza & Ghidella, 2012), led to tectonic crustal thickening and the expansion of the foreland basin (Encinas et al., 2019; Ramos, 1989). Marine sediments of the El Chacay Formation and equivalents were deposited in the late Oligocene - early Miocene and were interpreted as the onset of flexural subsidence (Figure 2;

Cuitiño et al., 2015) followed by fluvial sediments of the Santa Cruz Formation (18–14 Ma; U-Pb dating on zircon by Blisniuk et al., 2005; Cuitiño et al., 2015). Upper Miocene (12.4–10 Ma) flood basalts (Figure 2) associated with the PAW (Gorring et al., 1997; Guivel et al., 2006; Ramos, 1989) top the stratigraphic succesion. Neogene intrusive activity is represented by a series of granitic bodies that crop out in the retroarc (Figure 2) such as the Paso de las Llaves pluton (9.11 ± 0.11 Ma, U/Pb on zircon, Sánchez, 2011), and the San Lorenzo pluton (6.19 ± 0.12 Ma, ^{40}Ar/^{39}Ar on biotite, Welkner et al., 2002). After 7 Ma, widespread glaciers have shaped the landscape as recorded in preserved erosional and depositional glacial landforms (Coronato et al., 2004; Davies et al., 2020; Glasser et al., 2008).

The SPA can be subdivided into two N-S trending structural domains (Figures 1–3): a basement domain and a FTB. The western basement domain includes Paleozoic metasediments, the SPB, and El Quemado Complex. Its eastern boundary is characterized by a series of west-vergent faults interpreted as Jurassic normal faults, positively inverted in the Aptian-Cenomanian and later in the Miocene (Aramendía et al., 2018; Ronda et al., 2019) (Figures 2 and 3). The basement domain was affected by N-S-oriented dextral strike-slip faults like the Liquiñe-Ofqui fault zone, active since the Eocene (e.g., Cembrano et al., 1996; Hernandez-Moreno et al., 2014), and recently documented structures during the last 4 Myr (Georgieva et al., 2016, 2019). Out-of-sequence east-vergent thrusting may have affected the San Lorenzo granite (Figures 2 and 3), after 6 Ma (Ronda et al., 2019 after Ramos, 1989).

The external domain comprises the FTB to the east, including Cretaceous to Cenozoic sedimentary and volcanic rocks (Figures 1–3). A wide west-vergent frontal monocline can be found at its eastern boundary, linked to Miocene contractional deformation and overlain by undeformed <10 Ma basalts (Figure 3; Ronda et al., 2019).

3. Thermochronological Analyses

3.1. Method and Sampling Strategy

To assess the thermal histories of this part of the SPA we acquired 50 ZHe and 19 AFT new thermochronometric ages, collected from bedrock samples along two E-W oriented 200-km-long transects (Figures 2 and 3) across both structural domains, and covering glaciated and de-glaciated areas. The transects are close to the northern limit of the PAW (Figure 1). Additional ZHe ages were obtained for samples from a 2,300 m high elevation transect at Cerro Barrancos (Figure 2) which were previously analyzed using AFT (Haschke et al., 2006) and AHe (Guillaume et al., 2013). GPS sample locations, elevations and detailed analytical procedures used for thermochronological dating can be found in Text S1 and Text S2 in Supporting Information S1.

3.2. Apatite Fission Track Results

Nineteen bedrock samples yielded enough apatite grains to be analyzed and between 10 and 40 grains were dated in each sample (Table 1). Uranium content varied between 42 and 5 ppm, six samples had an average content <10 ppm and two samples were discarded because their content in Uranium <5 ppm precluded obtaining meaningful results. Except for two partially-reset sedimentary samples (RB1 and RB2), central ages ranged from 23.9 ± 4.3 Ma to 5.5 ± 0.9 Ma (Table 1; Figure 2).

Samples from Exploradores valley (Figure 2) yielded central ages of 8.8 ± 1.0 Ma, 8.0 ± 1.0 Ma, and 8.1 ± 1.2 Ma (Table 1) while at Caleta Tortel, central ages are slightly older at 13.1 ± 1.9 Ma, 13.3 ± 2.9 Ma, 13.5 ± 1.9 Ma, and 21.8 ± 4.0 Ma (Table 1, Figure 2).

Samples collected from different lithologies along the southern shore of Lago General Carrera-Buenos Aires yielded central ages ranging from 5.9 ± 0.9 Ma to 15.3 ± 3.0 Ma (Table 1, Figure 2). Sedimentary samples LGC8 and FUR1 from Miocene sandstones of the Guadal Formation from the Cosmelli basin yielded well-grouped central ages of 5.9 ± 1.3 Ma and 5.5 ± 0.9 Ma with $P(\chi^2) > 93\%$ suggesting that these samples have been reset (Table 1; Figure 2). Sample FUR2 collected in the younger Santa Cruz Formation was discarded due to low [U] ~5ppm and incoherence with a younger and more robust ZHe mean age.

In the Lago Belgrano area samples SU2 and JK1 obtained from late Paleozoic and Jurassic rocks yielded ages of 23.1 ± 5.4 Ma and 21.9 ± 3.3 Ma, respectively (Table 1; Figures 2 and 3). Further north, along the Lago Pueyrredón, Jurassic sample FRO1 yielded an age of 23.9 ± 4.3 Ma (Table 1; Figures 2 and 3). Sedimentary samples RB1 and RB2 collected in Aptian-Albian sandstones (U-Pb in detrital zircons, Ghiglione et al., 2015)

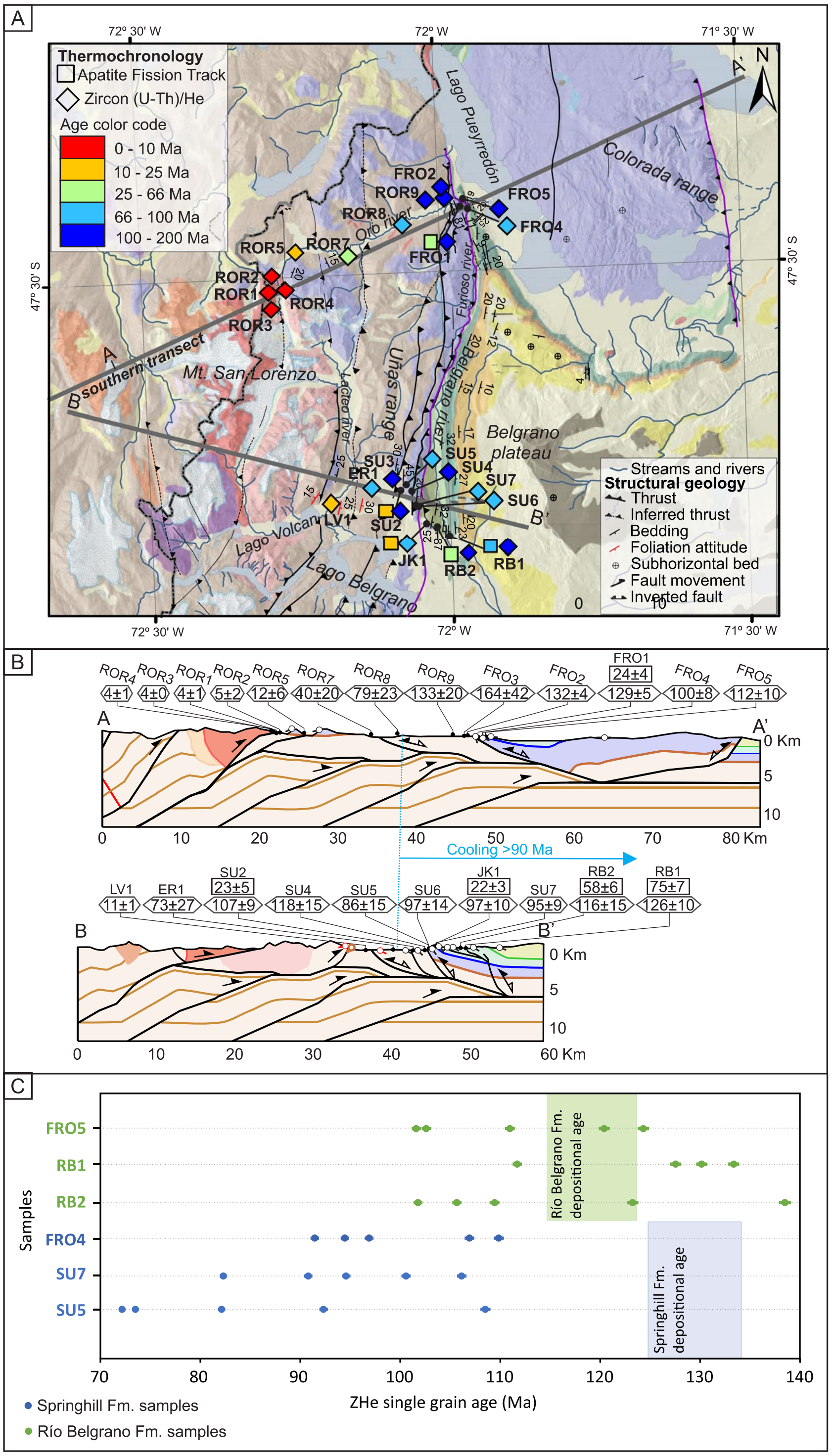

Figure 3. (a) Geologic map of the Lago Pueyrredón-Lago Belgrano area (modified from Ronda et al., 2019) with AFT and ZHe ages from this study. Geology references are the same as in Figure 2. (b) Cross sections and datasets modified from Ronda et al. (2019). Brown lines indicate basement rocks, light brown top of basement; blue lines, top of El Quemado Complex and equivalent units; green lines, top of the Cretaceous sedimentary rocks. Subsurface geometry is only constrained by surface geology and kinematic viability in Andino 3D (Cristallini et al., 2019). (c) Cretaceous sedimentary samples versus obtained single-grain ZHe ages. Samples from Hauterivian-Barremian Springhill Formation (SU5, SU7, FRO4) yielded ages younger than its depositional age while samples taken from Aptian Río Belgrano Formation (RB1, RB2, FRO5) exhibit larger spreading, with 50% ages older than its depositional age of 122 Ma (Ghiglione et al., 2015).

Table 1
Apatite Fission Track Results

Sample	Geological unit	Dated grains	Spontaneous tracks ($\rho_s \times E^6$ cm^{-2})	N_s	Induced tracks ($\rho_i \times E^6$ cm^{-2})	N_i	Dosimeter tracks ($\rho_d \times E^6$ cm^{-2})	N_d	$P(\chi^2)$	Central age ±1σ (Ma)	[U] (ppm)
EX1	SPB	20	0.1210	151	2.6650	3,326	1.1326	5,414	87	8.8 ± 1.0	31
EX2	SPB	20	0.1263	93	3.0988	2,375	1.1403	5,414	90	8.0 ± 1.0	36
EX3	SPB	16	0.0910	62	2.2244	1,515	1.1557	5,414	95	8.1 ± 1.2	29
TOR5	SPB	14	0.1121	40	1.0680	381	1.2096	5,414	56	21.8 ± 4.0	14
TOR6	SPB	22	0.0868	80	1.3442	1,159	1.2173	5,414	96	13.5 ± 1.8	16
TOR7	SPB	13	0.1149	40	1.9044	663	1.2251	5,414	7	13.3 ± 2.9	23
TOR8	SPB	22	0.2226	103	3.6029	1,667	1.2328	5,414	90	13.1 ± 1.7	42
LGC4	Intrusive	16	0.0699	33	0.9705	458	1.2405	5,414	77	15.3 ± 3.0	10
LGC5	Porphire	10	0.0147	17	0.3514	406	1.2482	5,414	98	9.0 ± 2.3	8
LGC6	Granodiorite	17	0.0732	104	2.5720	3,656	1.2559	5,414	99	6.1 ± 0.8	27
LGC7	Dike	20	0.0436	56	1.6064	2,064	1.2636	5,414	98	5.9 ± 0.9	17
LGC8*	Guadal Fm.	11	0.0264	24	0.9818	891	1.2713	5,414	93	5.9 ± 1.3	11
FUR1*	Guadal Fm.	25	0.0207	44	0.8337	1,776	1.2867	5,414	99	5.5 ± 0.9	9
FUR2*	Santa Cruz Fm.?	25	0.0331	61	0.6378	1,177	1.2982	5,414	98	11.5 ± 1.8	7
SU2	Río Lácteo Fm.	13	0.2280	41	2.1803	392	1.1711	5,414	14	23.1 ± 5.4	22
JK1	El Quemado Cpx.	20	0.0423	61	0.3846	582	1.1634	5,414	83	21.9 ± 3.3	5
RB1*	Río Belgrano Fm.	39	0.2388	464	0.6058	1,177	1.1095	5,414	9	75.2 ± 7.4	7
RB2*	Río Belgrano Fm.	40	0.3047	866	1.0305	2,929	1.1210	5,414	0	57.9 ± 5.6	12
FRO1	El Quemado Cpx.	12	0.0708	42	0.5464	324	1.0787	5,414	18	23.9 ± 4.3	7

Note. (*) Sedimentary Samples. N_s, number of spontaneous tracks per sample; ρ_s, spontaneous track density; N_i, induced track density; ρ_i, induced track density; N_d: number of tracks in dosimeters CN_5; ρ_d, dosimeter track density; $P(\chi^2)$, χ^2 percentage test, samples >5% are considered to contain grain ages from a single population of normal distribution; [U]: average U concentration.

in the Lago Belgrano area yielded ages of 75.2 ± 7.4 Ma and 57.9 ± 5.6 Ma. Low $P(\chi^2)$ values of 9% and 0%, respectively, indicate significant single-grain age dispersion attributed to partial resetting and low U content (Table 1; Figures 2 and 3). All these samples were collected from rocks deformed by west-verging faults as seen in Figure 3b, a fact that will be further analyzed in the discussion.

3.3. Zircon (U-Th)/He Results

A total of 250 grains from 50 bedrock samples (5 aliquots per sample; Text S1 and Text S2 in Supporting Information S1; Figure 2) were processed for ZHe thermochronology. Single-grain ages ranged between 3.6 Ma and 207.1 Ma. Mean ages were calculated from 4 to 5 aliquots except for samples SU6 and FRO2 for which two aliquots were discarded (Table 2 and Text S2 in Supporting Information S1). Outlier aliquots were discarded based on the distance from the sample's mean age, anomalous relationships between grain size versus age with respect to other aliquots, and inconsistencies between crystallization and cooling ages from a given unit. Sedimentary samples displaying higher dispersion of single grain ages were interpreted as being partially reset.

Samples TOR2 to TOR8 from the Caleta Tortel area (Figure 2) yielded mean ages between 16.5 ± 4.4 Ma and 27.0 ± 4.3 Ma (Table 2). Aliquot TOR5-1 showed a distance greater than 50% of the sample's mean age and was discarded as an outlier (Text S2 in Supporting Information S1). North of the North Patagonian icefield, samples EX1-EX2-EX3 gave mean ages ranging between 20.0 ± 1.5 Ma and 26.8 ± 4.1 Ma, overlapping the oldest ages obtained at Caleta Tortel, whereas sample EX4 yielded a younger age of 5.7 ± 0.7 Ma (Figure 2; Table 2). Aliquots EX1-5, EX3-2 were discarded as outliers due to their distance close to 50% relative to their mean age, whereas EX2-2 was discarded based on its age versus grain size relation (Text S2 in Supporting Information S1).

Table 2
Zircon (U/Th)/He Results

Sample (aliquots)	Mean He (nmol/g)	Mean U (ppm)	Mean Th (ppm)	Mean Sm (ppm)	Mean width (μm)	Mean raw age (Ma)	Mean Ft	Mean age (Ma)	Mean age STD (Ma)
TOR2 (5)	118.28	1,241.56	784.68	14.07	93.52	16.71	0.78	21.4	5.6
TOR3 (5)	68.27	714.77	593.95	20.00	102.68	14.47	0.80	18.2	4.4
TOR4 (5)	94.69	1,149.28	991.57	16.91	81.31	12.35	0.75	16.5	4.4
TOR5 (4)	25.90	232.76	147.75	3.68	92.67	16.54	0.78	21.2	4.4
TOR6 (5)	42.97	387.82	240.75	9.03	91.89	20.05	0.78	25.9	10.0
TOR7 (5)	35.22	357.12	561.37	10.76	109.76	14.12	0.81	17.5	3.2
TOR8 (5)	91.22	666.80	466.36	5.48	94.38	21.08	0.78	27.0	4.3
EX1 (5)	56.56	517.68	269.38	4.83	110.89	18.37	0.82	22.4	7.4
EX2 (4)	64.71	476.79	236.95	6.34	113.68	21.94	0.82	26.8	4.1
EX3 (4)	30.98	314.53	183.00	7.72	104.67	16.20	0.81	20.0	1.5
EX4 (5)	6.55	248.72	112.32	3.23	89.58	4.51	0.79	5.7	0.7
DES16 (4)	101.08	250.11	119.93	3.76	104.58	67.25	0.81	83.9	8.9
DES17 (4)	100.58	257.75	127.34	2.87	91.47	65.18	0.79	82.8	4.9
DES18 (4)	162.59	379.46	161.75	3.93	91.53	72.28	0.79	91.6	4.5
DES19 (4)	99.53	267.14	154.54	3.27	94.55	61.09	0.79	77.6	5.9
DES20 (5)	30.12	83.33	42.56	1.30	152.23	59.97	0.87	69.0	6. 7
DES21 (5)	69.18	195.38	108.27	2.66	100.92	57.97	0.80	72.1	3.9
DES22 (4)	56.67	170.66	102.33	2.44	110.46	55.77	0.81	68.3	4. 8
LGC1 (5)	180.00	304.60	177.79	9.46	103.43	98.61	0.79	124.9	13.1
LGC2 (5)	142.47	238.25	148.34	5.51	105.29	95.13	0.81	118.0	8.3
LGC3 (5)	120.24	225.94	151.24	8.17	86.27	86.25	0.77	112.5	9.4
LGC6 (5)	3.49	144.47	111.03	2.18	125.66	3.81	0.83	4.6	0.3
LGC7 (5)	122.44	308.24	82.30	3.84	110.35	69.69	0.83	84.0	16.4
LGC8 (5)*	48.66	243.69	141.59	1.82	98.54	23.93	0.80	30.0	27.6
FUR1 (4)*	6.69	129.51	90.05	3.70	94.27	7.72	0.80	9.7	1.4
FUR2 (4)*	3.70	108.69	63.89	2.59	94.17	5.22	0.78	6.6	1.9
RB1 (4)*	42.59	66.01	59.14	1.78	92.25	98.23	0.78	125.7	9.6
RB2 (5)*	148.15	249.57	111.88	3.25	110.54	95.20	0.82	115.7	15.1
JK1 (4)	149.16	325.55	143.58	6.46	94.12	77.97	0.80	97.3	9.5
SU2 (4)	81.40	163.11	105.76	49.77	79.83	79.91	0.75	106.9	8.8
SU3 (5)	97.99	177.07	112.12	5.69	100.70	85.15	0.80	107.2	15.7
SU4 (5)	120.29	221.98	132.67	10.30	81.31	88.97	0.76	117.7	15.3
SU5 (5)*	91.69	226.27	103.44	3.63	78.91	65.08	0.76	85.7	15.1
SU6 (3)	148.02	481.26	161.55	20.67	66.29	69.39	0.71	97.4	13.6
SU7 (5) *	98.28	203.64	99.02	3.94	110.89	78.14	0.82	94.9	9.1
ER1 (5)	126.95	327.80	103.71	8.29	81.45	64.19	0.76	86.3	37.4
LV1 (5)	14.80	300.87	117.29	2.20	90.12	8.27	0.78	10.6	1.1
ROR1 (5)	6.90	349.57	187.87	22.12	95.34	3.32	0.80	4.2	0.6
ROR2 (4)	6.72	297.69	131.23	39.74	89.17	3.97	0.77	5.2	1.6
ROR3 (5)	6.94	341.76	328.89	8.20	84.95	3.09	0.77	4.0	0.3
ROR4 (5)	8.26	378.48	267.92	11.99	102.46	3.40	0.81	4.2	0.5
ROR5 (4)	17.67	348.71	239.00	6.53	84.06	8.97	0.75	11.8	5.8

Table 2
Continued

Sample (aliquots)	Mean He (nmol/g)	Mean U (ppm)	Mean Th (ppm)	Mean Sm (ppm)	Mean width (µm)	Mean raw age (Ma)	Mean Ft	Mean age (Ma)	Mean age STD (Ma)
ROR7 (5)	53.38	274.79	151.68	47.09	92.56	31.95	0.79	40.4	20.2
ROR8 (5)	111.00	329.50	92.39	3.05	75.97	59.41	0.75	78.8	23.4
ROR9 (5)	135.31	219.06	125.60	48.87	82.10	101.23	0.76	133.4	20.3
FRO1 (3)	104.91	167.27	81.77	6.23	99.09	104.06	0.81	129.2	4.9
FRO2 (3)	175.80	270.72	126.28	3.95	101.49	108.14	0.82	132.5	4.2
FRO3 (5)	159.38	212.26	84.41	10.10	79.04	123.63	0.75	163.7	42.0
FRO4 (5)*	163.41	349.24	143.01	4.32	88.64	78.87	0.79	99.9	8.0
FRO5 (5)*	108.89	193.89	86.09	2.92	102.71	91.39	0.82	112.0	10.2

Note. (*) Sedimentary Samples. Number in brackets after sample name indicate the number of aliquots used to calculate the mean cooling age. Ft is α-ejection correction factor. Full data set can be found in Text S2 in Supporting Information S1.

Samples DES16-22 from the Cerro Barrancos granodiorite (123 ± 3 Ma, K-Ar on biotite, De la Cruz et al., 2004), were taken between 150 and 1,440 m elevation and separated by a horizontal distance of 4.5 km (inset in Figure 2). Aliquots DES16-4, DES17-4, DES18-1, DES19-4 DES22-4 were not used for the calculation of the mean age, despite not being considered outliers, due to its lower or higher eU versus age relations indicating a different closure temperature in comparison to other aliquots (Text S2 in Supporting Information S1). Samples yielded mean cooling ages between 68.3 ± 4.8 Ma at the base and 91.6 ± 4.5 Ma toward the top of the profile (Table 2; inset in Figure 2).

LGC6, collected from the Paso de las Llaves pluton (9 Ma, U-Pb on zircons; Sánchez, 2011), gave an age of 4.6 ± 0.3 Ma, more than 5 Myr younger than its crystallization age (Figure 2; Table 2). Sedimentary samples from the Guadal and Santa Cruz formations yielded variable results. Both FUR1 and FUR2 yielded clustered single grain ages with mean ages of 9.7 ± 1.4 Ma and 6.6 ± 1.9 Ma, respectively (Figure 2; Table 2) suggesting resetting. Aliquots FUR1-2 and FUR2-1 were discarded due to its difference, higher than 50%, from their mean ages. In contrast, sample LGC8, which was collected from a similar stratigraphic level to FUR1, provided a dispersed bimodal distribution and a meaningless mean age of 30.0 ± 27.6 Ma probably reflecting partial resetting, which was not plotted in Figures 2 and 3 (Text S1 in Supporting Information S1 and Table 2). Easternmost samples LGC1 to LGC3, taken from Jurassic pyroclastites, yielded mean ages of 112.5 ± 9.4 Ma to 124.9 ± 13.1 Ma (Figure 2; Table 2) younger than the stratigraphic age of 154.1 ± 1.5 Ma (U-Pb SHRIMP on zircons from El Quemado Complex, Pankhurst et al., 1999). LGC7 provided a mean age of 84.0 ± 16.4 Ma, with a bimodal distribution of single grain ages with peaks at 71.7 and 101.8 Ma (see Text S2 in Supporting Information S1) suggesting partial resetting.

In the southeastern part of the studied area, between Posadas and Belgrano lakes (Figures 2 and 3), a similar trend of mean ages, was observed: Cenozoic ages in the west and middle Cretaceous ages in the east (Figures 3 and 4). NE of the San Lorenzo granite, Cenozoic cooling ages were obtained from samples ROR5, ROR7 and LV1 of 11.8 ± 5.8 Ma, 40.4 ± 20.2 Ma, and 10.6 ± 1.1 Ma, respectively (Figures 2 and 3; Table 2). Aliquot ROR5-5 exhibited a distance >50% from the mean age and was discarded (Text S2 in Supporting Information S1). Slightly to the west, ROR1 to ROR4 yielded younger ages between 4.0 ± 0.3 Ma and 5.2 ± 1.6 Ma (Figures 2 and 3; Table 2) most of them postdating the San Lorenzo granite's crystallization age by 2 Myr (6.19 ± 0.12 Ma, ^{40}Ar/^{39}Ar in biotite, Welkner et al., 2002). Only aliquot ROR2-4 was discarded from this set considering its difference from the mean age (Text S2 in Supporting Information S1).

In the Lago Pueyrredón area samples ROR8 and ROR9 yielded mean ages of 78.8 ± 23.4 Ma and 133.4 ± 20.3 Ma, whereas samples FRO1 to FRO3 yielded mean ages between 129.2 ± 4.9 Ma and 163.7 ± 42.0 Ma after discarding aliquots FRO1-1, FRO1-3 and FRO2-1, older than the El Quemado Complex crystallization age (Figures 2 and 3; Table 2). Aliquot FRO2-5 was discarded due to a difference >50% relative to its mean age (Text S2 in Supporting Information S1). Sedimentary sample FRO4 (Springhill Fm.) yielded 99.9 ± 8.0 Ma, fully reset in relation to the Hauterivian/Barremian age of the unit (Figure 3c), whereas FRO5 (Río Belgrano Fm.) yielded a

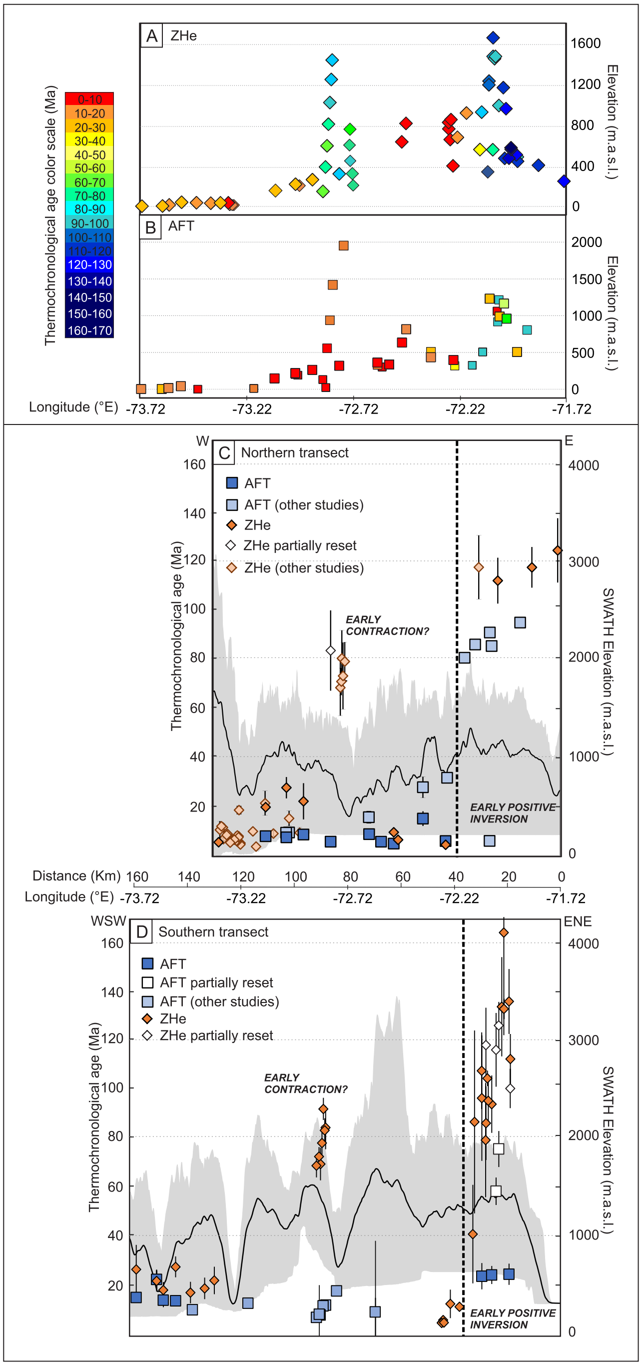

Figure 4. (a) ZHe mean ages (this study; Andrić-Tomašević et al., 2021) plotted (color-scale) in an elevation versus longitude space. (b) AFT central ages (this study; Haschke et al., 2006; Thomson et al., 2010; Andrić-Tomašević et al., 2021) plotted (color-scale) in an elevation versus longitude space. (c and d) Thermochronological ages plotted against distance from northern (c) and southern (d) transects analyzed (Figure 2), along with SWATH profiles. The latter display maximum (light gray), mean (black line), and minimum (white) topographies obtained from SRTM DEM (30 m resolution, accessed through CGIAR-CSI) and processed in Topotoolbox (Schwanghart & Scherler, 2014) with a 30 km strip width. Eastern extent of Last Glacial Maximum is east of both transects.

mean age of 112.0 ± 10.2 Ma (Figure 2, Figures 3a and 3b; Table 2). Aliquots FRO5-4 and FRO5-5 were close to or older than the ~122 Ma maximum depositional age of Río Belgrano Formation (Ghiglione et al., 2015), a trend that is also seen in other samples from this unit and that is interpreted as reflecting partial resetting of the ZHe system (Figure 3c). All these samples were obtained from positively inverted structures (Figure 3b).

North of Lago Belgrano, the Sierra de Uñas range is constituted by west-verging faults where synextensional Jurassic volcanics of El Quemado Complex evidence positive inversion, most likely during the Cretaceous and Miocene (Ronda et al., 2019, Figures 3a and 3b). In this region, sample's JK1-SU2 to SU4 and SU6 cooling ages were between 97.3 ± 9.5 Ma and 117.7 ± 15.3 Ma. Aliquots JK1-2 and SU2-4 were discarded due to their distance from clustered aliquots (Text S2 in Supporting Information S1). Aliquot SU6-4 exceeded the crystallization age of the unit and was discarded (Text S2 in Supporting Information S1). These samples displayed mean ages significantly younger than the crystallization age of El Quemado Complex at 154.1 ± 1.5 Ma (U-Pb SHRIMP on zircons, Pankhurst et al., 1999) (Figures 2 and 3; Table 2). Sedimentary samples taken from Springhill Formation (SU5 and SU7) yielded consistent mean ages of 85.7 ± 15.1 and 94.9 ± 9.1 Ma, all younger than their Hauterivian/Barremian depositional age (Ottone & Aguirre-Urreta, 2000) and are considered fully reset (Figure 2, Figures 3a–3c; Table 2). Sample ER1 showed a higher dispersion and a bimodal distribution yielding a mean age of 86.3 ± 37.4 Ma (Table 2). Sedimentary samples RB1 and RB2 provided similar mean ZHe ages of 125.7 ± 9.6 Ma and 115.7 ± 15.1 Ma (Figure, 2, Figures 3a-b; Table 2), from variably dispersed suites of single-grain ages (Figure 3c). Aliquot RB1-2 was discarded due to the distance to its mean age. Since several single-grain ages of these samples were older than ~122 Ma, maximum depositional age of the Río Belgrano Formation, they are considered partially-reset (Figure 3c).

3.4. Thermochronological Ages, Elevation and Longitude Correlations

In search of thermochronological age versus elevation and/or longitudinal correlations, we plotted, in an elevation versus longitude space, obtained and existing ZHe mean ages (Figure 4a) and AFT central ages (Figure 4b). Thermochronological ages were represented by a color-scale ranging from 0 to 170 Ma (Figures 4a and 4b). While an age-elevation correlation is evident in the ZHe Cerro Barrancos profile and expected considering that it is the only elevation profile sampled, it is not discernible for other ZHe or for AFT data (Figures 4a and 4b). Young ages are found at variable topographic levels, in some cases close to significantly older thermochronological ages. Age versus elevation correlations may thus be found locally within structural blocks, but do not seem to alter the overall longitudinal trends we observe (Figures 2–4).

To seek for other correlations, newly obtained and existing thermochronological ages were separated and plotted in a northern (Fig. 4c) and a southern transects (Figure 4d). A general eastward increasing cooling-age trend can be observed for AFT and ZHe in both transects (Figure 2, Figures 4a and 4b). ZHe data west of 72.2°W are in majority <30 Ma for both transects. The exceptions are sample LGC7 (partially reset), published ZHe ages (Andrić-Tomašević et al., 2021) in the northern transect (Figure 4a), and those from the Cerro Barrancos vertical profile in the southern transect (Figures 2 and 4b). The latter group of ages present similar ages and longitudes but highly dissimilar elevations: DES samples are between 147 and

1,436 m.a.s.l. while LGC7 was taken at 319 m.a.s.l. This group may reflect Cretaceous cooling among a similar structural block during early positive inversion (Figures 2 and 4).

A sharp limit in cooling ages was recognized at 72.2°W, where samples LGC6 and ROR1 to ROR4 yielded ZHe ages <6 Ma (Figures 2 and 4). These samples were taken from two Miocene retroarc intrusives 60 Km apart from each other (Figure 2): LGC6 from Paso de las Llaves pluton (9 Ma, U-Pb on zircons; Sánchez, 2011), yielded a mean age of 4.6 ± 0.3 Ma, more than 5 Myr younger than its crystallization age (Figure 2; Table 2), whereas ROR1 to ROR4 were taken from the San Lorenzo granite (6.19 ± 0.12 Ma, ^{40}Ar/^{39}Ar in biotite, Welkner et al., 2002) and yielded mean ages between 4.0 ± 0.3 Ma and 5.2 ± 1.6 Ma (Figures 2 and 3; Table 2) most of them postdating the crystallization age by 2 Myr. The obtained ZHe ages are coherently younger than the reported crystallization ages of the sampled units. The lag-time between crystallization and ZHe cooling ages of 5 Myr for LGC6 and of 2 Myr for ROR1-ROR3-ROR4 combined with the longitudinal and cooling-ages coherence of both samples (Figures 2 and 4) could point to an independent cooling process other than intrusion cooling such as exhumation. Still, the intrusion of these plutons most likely influenced, under the form of thermal resetting, nearby samples like ROR5-ROR7 and LGC4-FUR1-FUR2-LGC8 (Figures 2–4).

East of 72.2°W, where positively inverted structures prevail, ZHe ages are almost entirely Cretaceous and older than 100 Ma (Figures 3 and 4a–b). AFT data are also oldest east of 72.2°W, most of them between 25 Ma and 50 Ma, whereas to the west AFT data provided ages <25 Ma, in both transects (Figures 4b–4d). The cooling-ages trends described can be similarly observed in the two analyzed transects (Figures 4c and 4d), hampering the recognition of an evident north-south variability in cooling ages in the studied area.

4. Thermal Modeling

4.1. Thermal Modeling Using *HeFty* Software

We performed 1D thermal inversion modeling of 12 single samples to estimate time-temperature histories (T-t paths) using *HeFTy* (Ketcham, 2005). By means of a Monte Carlo search, 50,000 iterations were run for each model. The random search was conducted using intermediate and monotonic variable half-segments to allow cooling and heating trajectories. This software allows us to insert geological constraints into the search space, and we included known crystallization and depositional ages of modeled rock units and known burial periods as constraints in models FUR1, JK1, FRO1, and LGC2 (Table 3). Additionally, we included wide constraints representing obtained thermochronological ages as a starting condition for igneous samples of unknown age (models EX1 to EX4, TOR7, TOR8; Table 3) or to enhance the search without overconstraining the modeling (FUR1 and THC17; Table 3). The present temperature was set to 10 ± 10°C. The diffusion models used included Guenthner et al. (2013) for ZHe data, Farley (2000) for AHe data, and Ketcham et al. (2007) for AFT data. We introduced all available single-grain ZHe ages, leaving out discarded aliquots, as inputs for modeling samples EX2, EX3, FUR1, LGC2, THC17, JK1, and FRO1. In the rest of the models, EX1-EX4-TOR7-TOR8-LGC7, 4 to 3 ZHe single-grain ages were used leaving out the most distant aliquots from their mean ages to improve convergence due to the absence of good paths when introducing all the aliquots (Table 3, Text S3 in Supporting Information S1). We used AFT single-grain data as inputs (Text S2 and Text S3 in Supporting Information S1). AHe and ZFT data were included as reported in their source publication (Text S3 in Supporting Information S1). For additional details on the annealing kinetic and diffusion models, input data and modeling parameters selected, see Table 3 and Text S3 in Supporting Information S1.

Samples collected from the SPB in the Exploradores valley (Figure 2) yielded monotonic to two-step cooling paths (Figure 5). EX1 resulted in monotonic cooling at 7°C/Ma during the past 23 Ma, with a minor increase during the last 6 Ma (Figure 5, Table 3). EX2 and EX3 showed an initial step of slow cooling between 30 Ma and 7–8 Ma at rates of 2–4°C/Ma and a second faster cooling stage after 7–8 Ma at rates of 10–14°C/Ma (Figure 5, Table 3). The EX4 modeling results showed a fast-cooling stage after 6 Ma at a rate of 20°C/Ma (Figure 5, Table 3). Samples TOR7 and TOR8 from Caleta Tortel (Figure 2), collected from the Patagonian Batholith, yielded lineal cooling during the past 26 Ma to the present at rates of 5–8°C/Ma (Figure 5, Table 3).

Samples LGC7, THC17 and FUR1, located east of the Exploradores valley (Figure 2), yielded differing results. Sample LGC7 collected from a felsic dyke that intruded the Paleozoic basement (Figure 2) indicates mild heating from 73 to 8 Ma followed by cooling at 14°C/Ma after 8 Ma. This model suggests that the rock unit sampled may be Cretaceous due to its residence at low temperatures since >73 Ma, and that ZHe data may reflect intrusion

Table 3
HeFTy Thermal Model Constraints and Results

Sample	EX1	EX2	EX3	EX4	TOR7	TOR8	LGC7	THC17	FUR1	LGC2	JK1	FRO1
Constraint 1	27–19 Ma	33–23 Ma	22–15 Ma	7–4.5 Ma	20–13 Ma	29–20 Ma	90–60 Ma	135–120 Ma	24–18 Ma	160–140 Ma	160–140 Ma	160–140 Ma
	220–100°C	220–80°C	220–80°C	220–20°C	220–80°C	220–80°C	220–40°C	240–120°C	40–0°C	40–0°C	40–0°C	40–0°C
Constraint 2	-	10–4 Ma	-	-	-	-	18–0 Ma	43–25 Ma	12–6 Ma	140–90 Ma	140–90 Ma	140–90 Ma
		140–60°C					160–0°C	120–40°C	220–80°C	240–20°C	240–100°C	240–60°C
Constraint 3	-	-	-	-	-	-	-	11-4 Ma	-	-	40-10 Ma	-
								97-40°C			180-40°	
Input summary	3ZHe-AFT-AHe	4ZHe-AFT-AHe	4ZHe-AFT-AHe	4ZHe-AHe	4ZHe-AFT	4ZHe-AFT-AHe	3ZHe-AFT	ZFT-AFT-AHe	4ZHe-AFT	5ZHe	4ZHe-AFT	3ZHe-AFT
Paths	50,000	50,000	50,000	50,000	50,000	50,000	50,000	50,000	30,000	50,000	50,000	50,000
Acceptable fits	2,482	1,341	386	5,584	10,796	857	1,535	512	1,407	5,727	965	809
Good fits	735	21	18	1,231	439	47	624	44	377	2,443	69	290
Cooling/heating Timing and rates	23–0 Ma	29–7 Ma	20–8 Ma	6–0 Ma	15–0 Ma	27–0 Ma	73–8 Ma	130–33 Ma	21–11 Ma	150–119 Ma	150–113 Ma	150–116 Ma
	7°C/Ma	2°C/Ma	4°C/Ma	20°C/Ma	8°C/Ma	5°C/Ma	−0.3°C/Ma	1°C/Ma	−17°C/Ma	−5°C/Ma	−5°C/Ma	−4°C/Ma
	-	7–0 Ma	8–0 Ma	-	-	-	8–0 Ma	9–0 Ma	11–0 Ma	119–0 Ma	113–80 Ma	116–15 Ma
		14°C/Ma	10°C/Ma				14°C/Ma	8°C/Ma	16°C/Ma	2°C/Ma	2°C/Ma	1°C/Ma
	-	-	-	-	-	-	-	-	-	-	22–0 Ma	15–0 Ma
											4°C/Ma	4°C/Ma
ZHe goodness of fit								0.70 (ZFT)		1.00		
		0.88	0.92	0.95	0.79	0.89	0.97		0.98	0.88	0.98	0.98
	0.99	0.42	0.60	0.73	0.65	0.67	0.90		0.90	0.87	0.67	0.84
	0.79	0.23	0.34	0.64	0.39	0.43	0.53		0.88	0.83	0.55	0.47
	0.26	0.16	0.25	0.65	0.17	0.14			0.48	0.17	0.30	
AFT goodness of fit	0.91	0.77	0.24	-	0.99	0.79	0.96	0.91	0.90	-	0.88	0.99
AHe goodness of fit	0.95	0.99	0.95	0.97	-	0.97	-	0.87	-	-	-	-

Note. Published and new ZHe, AHe, and AFT data used as inputs and are listed in Text S3 in Supporting Information S1. Constraints rationale can be found in main text. Cooling/heating rates were calculated from mean path. Goodness of fit was obtained from best-fit path and is a statistical comparison between measured and modeled ages where 1 is maximum and 0 is minimum fit.

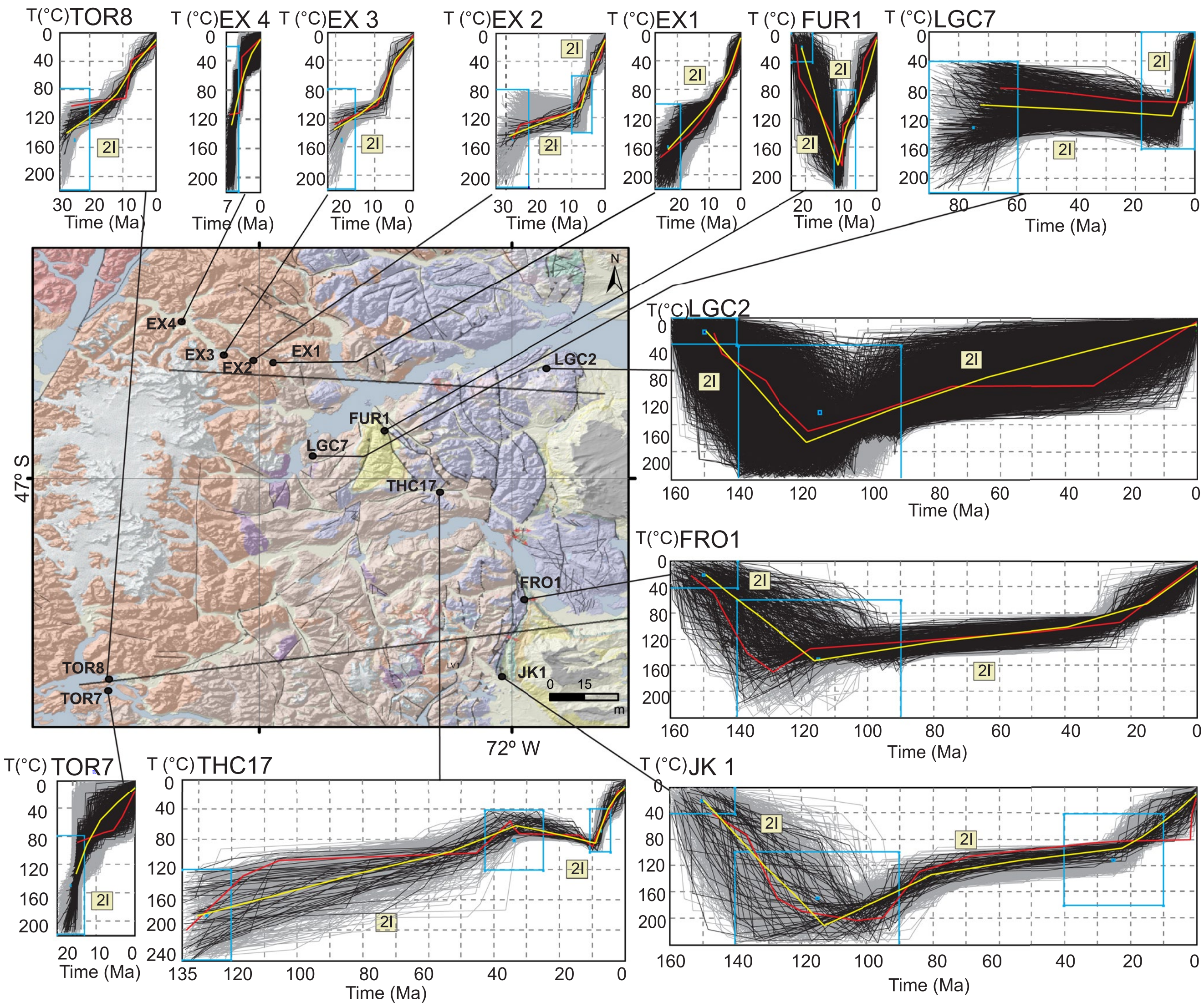

Figure 5. Inverse thermal modeling results of 11 samples from this study and sample THC17 from Thomson et al. (2010). Samples are bedrock, except for sedimentary FUR1. Models were processed using *HeFTy* software (Ketcham, 2005), and details on input data and modeling parameters are provided in Table 3 and Text S3 in Supporting Information S1. Light and dark gray lines are acceptable and good T-t paths, respectively. The yellow path represents the mean weighted path, and the red path represents the best fit path. Light blue boxes are T-t constraints. Black lines in map represent transects analyzed in Figures 2 and 4.

cooling. Sample THC17, collected from a granodiorite of the Patagonian Batholith with a zircon fission track cooling age of 126 ± 7 Ma (Thomson et al., 2010) showed slow cooling at 1°C/Ma between 130 and 33 Ma, with increased rates of 8°C/Ma after 9 Ma (Figure 5, Table 3). Reset sedimentary sample FUR1, collected from the Guadal Formation (Figure 2), was modeled including an initial constraint reflecting Miocene deposition (23-20 Ma U–Pb max. depositional age, Encinas et al., 2019). According to the model, it was heated to 180°C at 17°C/Ma between 21 and 11 Ma, and recorded cooling after 11 Ma at 16°C/Ma (Figure 5, Table 3). Burial alone cannot account for such a heating rate considering the sample's Miocene age and <1 km sedimentary cover. A regional thermal gradient increase also seems to be an unlikely explanation since it should have been recognized in other obtained thermal histories and not just FUR1, as shown in Figure 5. Most likely, the nearby Paso de las Llaves intrusion (Figure 2) aged 9.1 Ma (U–Pb on zircons; Sánchez, 2011), similar to the FUR1 ZHe mean age of 9.7 Ma, could have provided additional heating leading to thermal resetting of this sample (Figure 2; Table 2).

Samples located east of 72.2°W, collected from Jurassic volcaniclastic rocks of the El Quemado Complex, were modeled including an additional constraint based on a crystallization age of 154.1 ± 1.5 Ma obtained in the study area (Pankhurst et al., 1999) (Table 3). Sample LGC2 indicates heating at 5°C/Ma between extrusion and the beginning of cooling at ~119 Ma (Figure 5, Table 3), followed by an average cooling rate of 2°C/Ma to the present. The best-fit path shows a two-step cooling between 119 and 75 Ma, and after 31 Ma. Samples JK1 and FRO1 (Figure 2) display similar thermal histories including heating from 150 Ma to 113 Ma and 116 Ma, respectively, followed by cooling (Figure 5). JK1 recorded cooling between 113 and 80 Ma at 2°C/Ma and from 22 to 0 Ma at 4°C/Ma (Figure 5). FRO1 displayed monotonous cooling between 116 and 15 Ma at 1°C/Ma, accelerated to 4°C/Ma after 15 Ma. According to its best-fit path, cooling might have taken place at higher rates between 129 and 117 Ma and after 23 Ma.

In summary, for the thermochronological systems analyzed, samples collected from the SPB indicate an Oligocene-Miocene (30–7 Ma) cooling stage at <7°C/Ma and an increase in cooling rates over 10°C/Ma after 8 Ma. This fast-cooling episode was also observed in samples LGC7, THC17, and FUR1 further east toward foreland areas (Figure 5). East of 72.2°W, samples from the Jurassic El Quemado Complex (Figure 5) were reheated to 160–200°C and then cooled slowly between ~120 and 80 Ma; this slow cooling interval was also shared by the oldest part of the T-t paths of hinterland sample THC17. The eastern samples experienced final cooling starting at ~20 Ma (Figure 5).

4.2. Inverse Thermal Modeling of Sedimentary Bedrock Samples

We also used an inverse thermal-modeling approach to extract thermal histories from partially reset Cretaceous sedimentary samples RB1-RB2-FRO5 obtained from the Río Belgrano Fm (Figures 3a–3c). Inputs for modeling included obtained ZHe single-grain ages except for discarded aliquots (Text S2 in Supporting Information S1), hence the several ZHe GOF parameters reported in Figure 6. AFT single-grain ages were also introduced for RB1 and RB2 (Text S2 in Supporting Information S1). We set a series of geological constraints based on the U–Pb detrital zircon populations obtained for Río Belgrano Fm. by Ghiglione et al. (2015), which mark a maximum depositional age of 122 Ma and a main detrital peak of 180 Ma. A first box between 200 and 120 Ma and 250–300°C represents the history of both inherited and juvenile zircons between such ages starting at higher temperatures than those typical of the analyzed thermochronometers (Figure 6, Text S3 in Supporting Information S1). A box at surface temperatures between 130 and 115 Ma represents the deposition of the Río Belgrano Fm. sediments, followed by burial-related heating, to unknown temperatures (Figure 6, Text S3 in Supporting Information S1). A constraint was included between 50 and 30 Ma close to surface temperatures (Figure 6, Text S3 in Supporting Information S1) to represent the unconformity that separates the Rio Belgrano and Río Tarde formations from the Eocene Posadas Basalt in the area (see Section 2.2). Due to a high convergence, the ending condition of the models was set to 100 good-paths.

The models showed a large consistency when analyzing mean paths (Figure 6). Although highly unconstrained by the models, predepositional cooling must have taken place prior to the depositional age, and may have started between 158 and 146 Ma until 122–120 Ma, at 10–7°C/Ma according to the mean paths (Figure 6). Heating followed until 94–91 Ma at rates of 5–4°C/Ma (Figure 6). Samples reached temperatures between 120 and 170°C (Figure 6) within the ZHe partial-retention zone (Ault et al., 2019), which sustains the partial resetting suggested by ZHe single-grain ages (Figure 3c). Final cooling began at 94–91 Ma and took place at rates of 1–2°C/Ma (Figure 6). The models show no record of enhanced Oligocene-Miocene cooling, probably because the rocks were already close to the surface after the Eocene and indicate residence at surface temperatures until the present (Figure 6).

4.3. Cerro Barrancos Elevation Transect

As previously described, the ZHe ages of the Cerro Barrancos elevation transect ranged between 68.3 ± 4.8 Ma at the base and 91.6 ± 4.5 Ma (Table 2) toward the top of the profile and follow a coherent correlation of elevation and cooling ages (Figures 3a and 6a). We conducted a weighted error linear interpolation of the ZHe mean and single-grain ages that yielded a putative exhumation rate of 0.06 mm/yr for the time interval 89–64 Ma, slower than rates constrained by AFT and AHe data after 20 Ma (Figure 6a). We observed a hiatus in cooling ages relative to the AFT and AHe systems between 17.1 ± 1.2 Ma and 68.3 ± 4.8 Ma (Figure 6a), suggesting stagnation in cooling processes.

To test plausible T-t trajectories for the samples of Cerro Barrancos we conducted multisample inverse thermal modeling in *QTQt* (Gallagher, 2012). Modeling inputs include ZHe (this study), AHe (Guillaume et al., 2013)

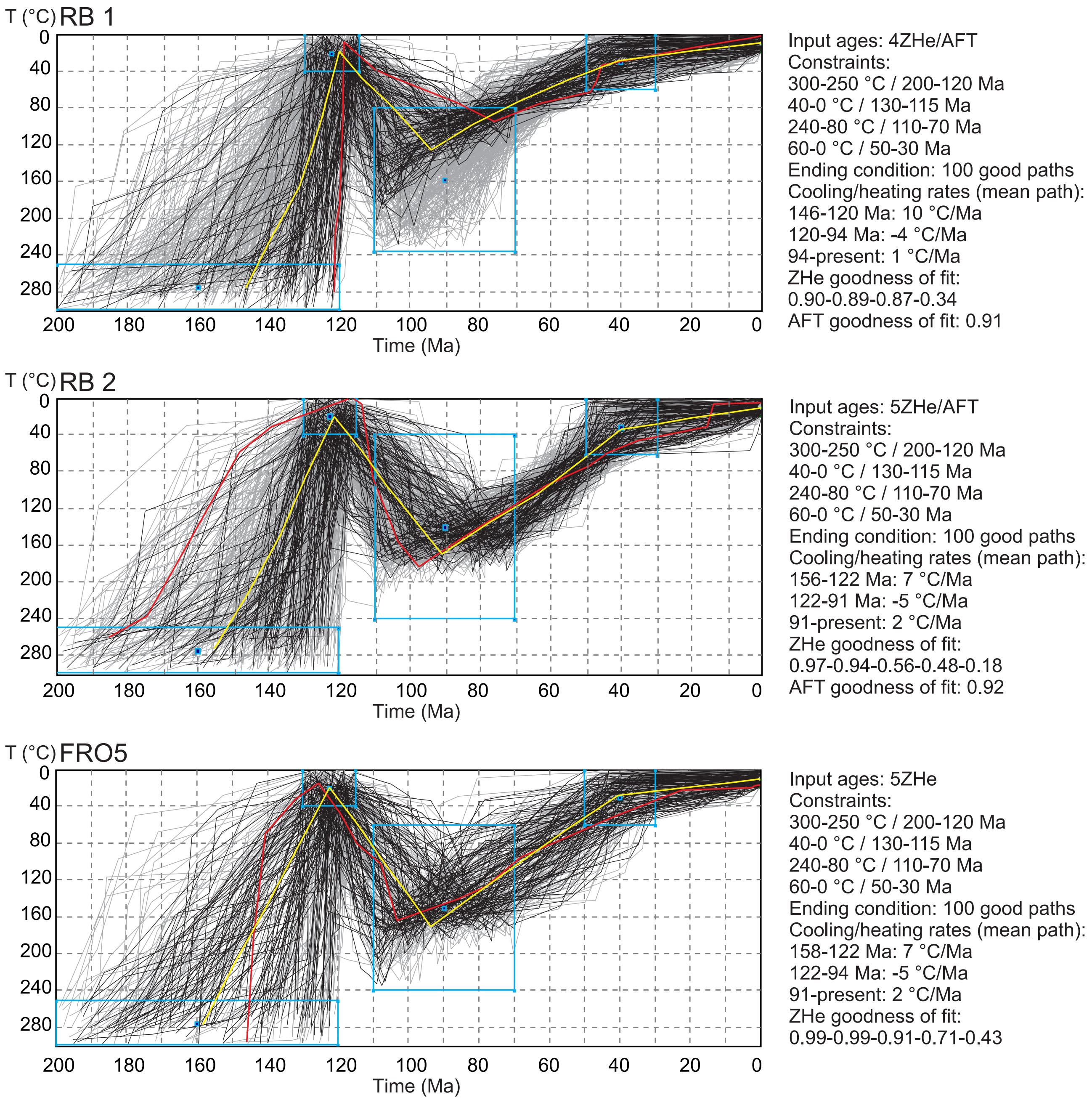

Input ages: 4ZHe/AFT
Constraints:
300-250 °C / 200-120 Ma
40-0 °C / 130-115 Ma
240-80 °C / 110-70 Ma
60-0 °C / 50-30 Ma
Ending condition: 100 good paths
Cooling/heating rates (mean path):
146-120 Ma: 10 °C/Ma
120-94 Ma: -4 °C/Ma
94-present: 1 °C/Ma
ZHe goodness of fit:
0.90-0.89-0.87-0.34
AFT goodness of fit: 0.91

Input ages: 5ZHe/AFT
Constraints:
300-250 °C / 200-120 Ma
40-0 °C / 130-115 Ma
240-80 °C / 110-70 Ma
60-0 °C / 50-30 Ma
Ending condition: 100 good paths
Cooling/heating rates (mean path):
156-122 Ma: 7 °C/Ma
122-91 Ma: -5 °C/Ma
91-present: 2 °C/Ma
ZHe goodness of fit:
0.97-0.94-0.56-0.48-0.18
AFT goodness of fit: 0.92

Input ages: 5ZHe
Constraints:
300-250 °C / 200-120 Ma
40-0 °C / 130-115 Ma
240-80 °C / 110-70 Ma
60-0 °C / 50-30 Ma
Ending condition: 100 good paths
Cooling/heating rates (mean path):
158-122 Ma: 7 °C/Ma
122-94 Ma: -5 °C/Ma
91-present: 2 °C/Ma
ZHe goodness of fit:
0.99-0.99-0.91-0.71-0.43

Figure 6. Inverse thermal modeling results of detrital samples RB1-RB2-FRO5 obtained from Río Belgrano Formation (see Figure 3). Models were processed using *HeFTy* software (Ketcham, 2005), further details on input data and modeling parameters are provided in Text S3 in Supporting Information S1. Light and dark gray lines are acceptable and good T-t paths, respectively. The yellow path represents the mean weighted path, and the red path represents the best fit path. Light blue boxes are T-t constraints. Constraints rationale can be found in main text.

and AFT ages (Haschke et al., 2006), except for sample CB-1960 due to its lack of AHe and ZHe data. Most of the ZHe samples showed a negative eU versus age correlation (Text S2 in Supporting Information S1), indicating that obtained aliquots fall within one of the available damage radiation models (Guenthner et al., 2013). To reflect the variable radiation damage of the samples in the modeling procedure all the aliquots were used for modeling, even those that were not used for mean age calculation.

QTQt makes use of Markov chains to minimize the difference between observed and modeled ages derived from time-temperature paths (Gallagher, 2012). The convergence of the models is assessed through the consistency between iterations, the larger the consistency is, the stronger the convergence in the likelihood chain. Four models were performed until the maximum likelihood chain showed a stable uniform trend, which was reached after >200,000 paths (plot in Text S3 in Supporting Information S1). An initial time-temperature search space was defined by a series of priors including prior time (92 ± 92 Ma, related to the oldest sample of the profile; Text S3 in Supporting Information S1) and prior temperature (150 ± 150°C, a range that includes the typical sensitivity of the thermochronometers used; Ault et al., 2019; Text S3 in Supporting Information S1). Additionally, for multisample vertical profiles, an initial temperature offset between the uppermost and lowermost samples had to be defined by setting a geothermal gradient, which was set to 30°C/km considering that the area was a foreland region under plunging subduction similar to other Andean foreland areas, at ~92 Ma (Text S3 in Supporting Information S1). As a starting condition we set an initial time-temperature constraint between 120 and 70 Ma, broadly based on the Cerro Barrancos 123 ± 3 Ma age (K-Ar on biotite, De la Cruz et al., 2004) and 250–300°C, above the typical sensitivity of the ZHe system. A second constraint between 0 Ma and 20–0°C reflected the present day mean annual surface temperature (Figure 7b). Further information on the modeling setup can be found in Text S3 in Supporting Information S1.

Modeling shows two cooling intervals between 85 and 75 Ma at 17°C/Ma, and after 6 Ma at 13°C/Ma (Figure 7b). The model suggests a long phase of heating of approximately 30°C between ~75 and 25 Ma, at 1°C/Ma, interpreted as protracted residence between 120 and 40°C, followed by mild cooling after 25 Ma (Figure 7b). A broad 95% confidence interval was obtained between 90 and 30 Ma, related to the lack of constraints other than ZHe cooling ages, bolstered by an internal uncertainty related to single grain age input (Figure 7b). Such an interval only constrains rapid cooling and a switch to reheating or stagnation at ~75 Ma (Figure 7b). The observed data are in good agreement with the model predictions, where most of the observed cooling ages ±1σ overlap with the predicted cooling ages for the three thermochronometers used (Figure 7c).

5. Discussion

5.1. Cretaceous Onset of Andean Deformation Revealed by ZHe Thermochronology: Intraplate Contraction?

Evidence for the Cretaceous onset of Andean shortening in the SPA is rather indirect, and includes anisotropy of magnetic susceptibility studies recording Cretaceous soft-sediment deformation (Aramendía et al., 2018) and palaeotopographic analyses (Colwyn et al., 2019). Likewise, Aptian-Cenomanian coarse continental sedimentation, and the angular unconformity with respect to Cenozoic rocks in the eastern FTB have been related to Cretaceous shortening (Aramendía et al., 2018; Ronda et al., 2019).

The ~120 Ma to ~80 Ma cooling phase recognized from thermal modeling of samples collected in the FTB is coeval with the proposed contractional deformation in the northern SPA (Figure 8). A switch from heating to cooling occurred between 120 and 90 Ma as shown in *HeFty* models LGC2, FRO1, JK1 (Figure 5), and in sedimentary sample models RB1-RB2-FRO5 (Figure 6). Since no Cretaceous crustal thermal events are registered in the area, the simplest explanation for the heating phase is sedimentary burial in a foreland basin as suggested by Ghiglione et al. (2015). The Cretaceous cooling signal is mostly preserved east of 72.2°W (Figures 2–4), where it spatially correlates with the occurrence of inverted normal faults and the angular unconformity between Cenomanian and Eocene rocks (Ronda et al., 2019). Cretaceous cooling is thus interpreted as a result of rock uplift in response to thrusting, folding and surface erosion. Model THC17 indicates ongoing cooling after 135 Ma (Figure 5). Samples LGC2, JK1, and LGC7 show stagnation in their thermal histories after 80 Ma (Figure 5).

The Cerro Barrancos ZHe ages, along with LGC6 and ZHe ages reported by Andrić-Tomašević et al. (2021) older than 50 Ma west of 72.2°W, are interpreted as recording an older cooling event probably linked to the early onset of contraction in this part of the orogen, where ZHe cooling ages are mostly younger than 30 Ma (Figures 2–4). The modeling results of the Cerro Barrancos vertical profile also show cooling after 100 Ma and heating to stagnation after 80 Ma (Figure 7). Gentle reheating to stagnation is the simplest explanation considering the poor burial implied by the extended upper Cretaceous hiatus to the east.

Our results also show that Hauterivian/Barremian sedimentary rocks of the Springhill Formation experienced total resetting according to its single-grain ZHe ages and thermal models (Figure 3c), whereas the overlying Aptian sedimentary rocks of the Río Belgrano Formation show partially reset to unreset cooling ages, some older than its maximum depositional age of 122 Ma (Ghiglione et al., 2015) (Figure 3c). Partial resetting of samples

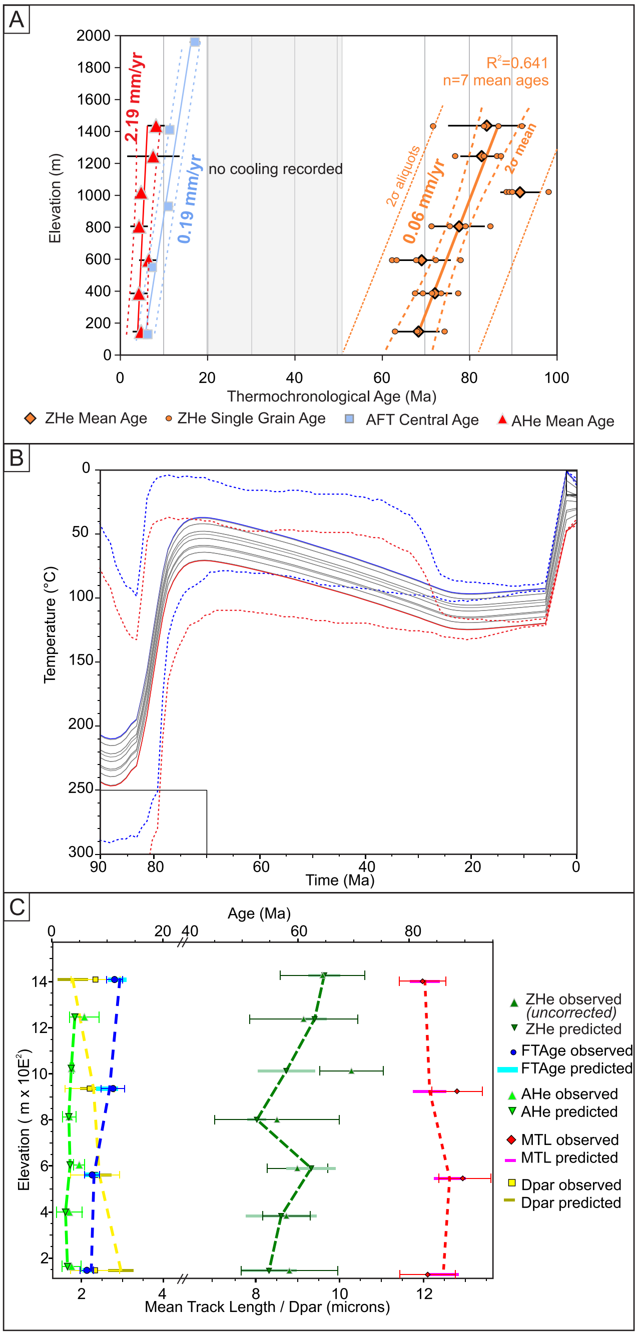

Figure 7. Cerro Barrancos thermochronological results. (a) AHe (Guillaume et al., 2013), AFT (Haschke et al., 2006) and ZHe (this study) elevation transects. Colored lines represent standard deviation-weighted mean ages linear regression (ZHe) and mean ages linear regressions (AFT and AHe). Dashed lines represent 2σ (for ZHe mean and single-grain age regression) and 1σ (AHe and AFT) intervals for linear regressions. (b) Results from multisample inverse thermal modeling using *QTQt* for the Cerro Barrancos vertical profile. The upper plot shows the expected (weighted mean) model time–temperature trajectories for the uppermost (blue) and lowermost (red) samples of the vertical profile, along with thermal histories for all samples in-between (gray). Blue and red dashed lines indicate the 95% confidence intervals for the uppermost and lowermost samples, respectively. Black boxes mark introduced constraints representing crystallization ages. (c) Observed versus predicted data comparison for the input datasets. MTL: mean track length, AHe: apatite (U–Th)/He; AFT: apatite fission track data. For prior modeling conditions, constraints, and modeling parameters the reader is referred to Text S3 in Supporting Information S1.

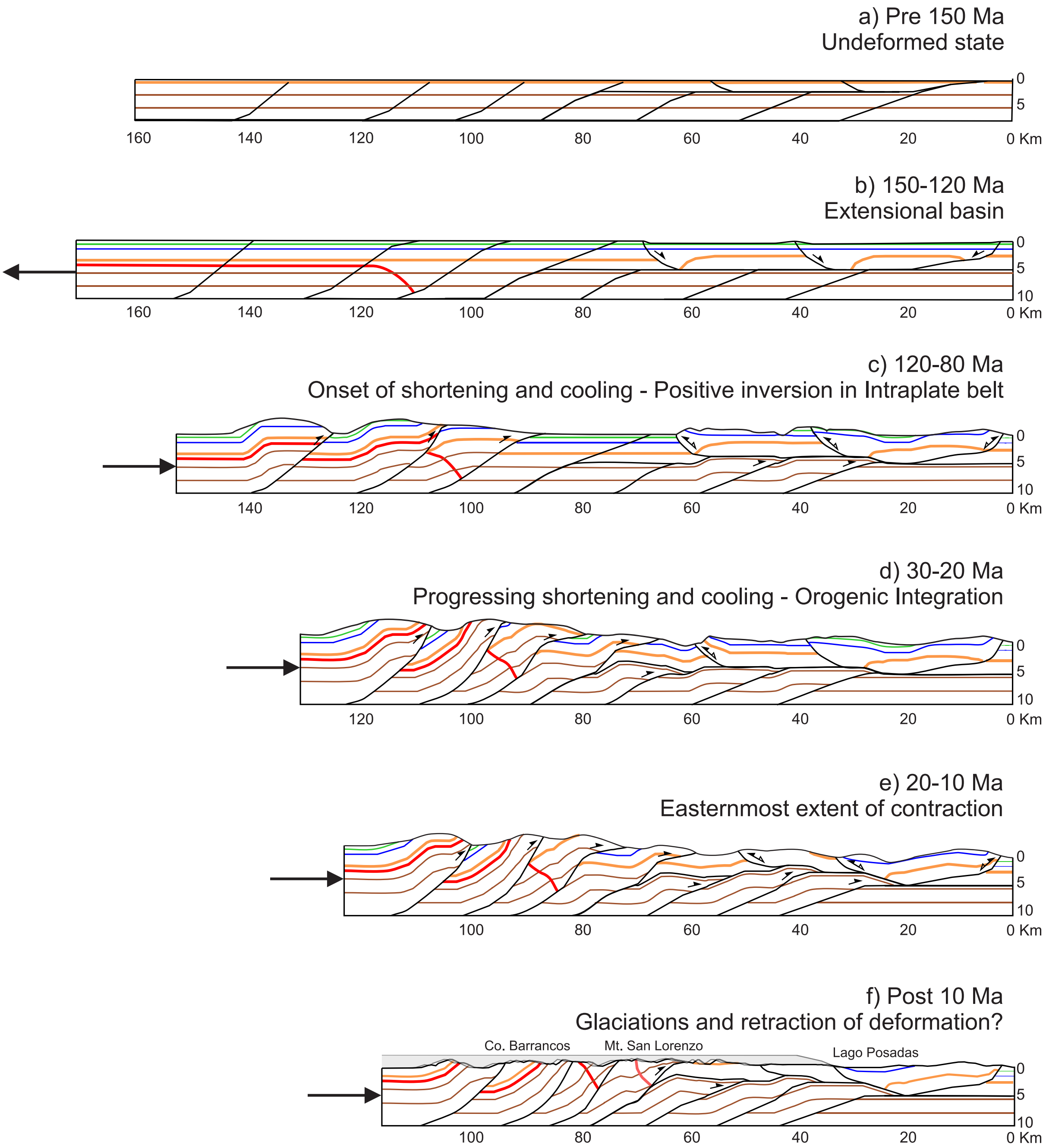

Figure 8. Forward model of a part of the southern transect (see Figure 2) using Andino 3D software. Brown lines indicate basement rocks, light brown top of basement; red lines, broadly represent intrusives of the Patagonian Batolith; blue lines, top of El Quemado Complex and equivalent units; green lines, top of the Cretaceous sedimentary rocks. (a) Undeformed state (b) Precontractional setting, extensional basin. (c) Initial contraction, cooling, and basin inversion generating an intraplate belt. (d) Eastwards progressing Oligocene-Miocene shortening and cooling. (e) Easternmost contraction and cooling, cessation of contraction at 10 Ma. (f) Onset of glaciations and postulated out-sequence thrusting during the past 10 Myr.

from the Río Belgrano Fm. is also sustained by inverse models that indicate burial to 120–170°C until 90 Ma when final cooling began (Figure 6). Since resetting was associated with burial, the switch to partially reset and unreset sedimentary samples suggests a decreasing burial rate during the Barremian/Aptian.

The initiation of the Cretaceous cooling phase at ∼120 Ma as shown by models FRO1-LGC2-JK1 (Figure 5), could be explained by a proposed shallow subduction phase linked to an eastward arc expansion in Patagonia at 46°–48°S, that would have taken place between ∼121–117 Ma and 84–82 Ma (Gianni et al., 2018). As a result, coupling between the Aluk-South America plates increased, promoting intraplate shortening reported east of the study area in the Deseado Massif (Figure 1) after the Barremian-Aptian (Giacosa et al., 2010; Gianni et al., 2018) and in the San Bernardo FTB (Figure 1) during the late Early Cretaceous (Gianni et al., 2015). The onset of shortening in the area would have been accompanied by the onset of rock uplift and cooling. In addition, shallow subduction might have enhanced crustal cooling by mantle wedge removal during the Late Cretaceous, as suggested for present settings like the Pampean flat slab (Dávila & Carter, 2013).

Although models FRO1-LGC2-JK1 indicate the onset of cooling at ∼120 Ma according to the mean paths, the variability in the best-fit paths suggests that cooling may not be entirely well constrained (Figure 5). Younger cooling trajectories starting at 100 Ma were still classified as good paths, sustaining the interpretation that cooling started at ∼100 Ma. The initiation of the Cretaceous cooling phase at 100 Ma could be explained by a plate reorganization event that included the separation and drift stage between South America and Africa. This led to the onset of westward motion of southernmost South America with respect to Africa at ∼100 Ma, as derived by paleomagnetic studies in the eastern San Bernardo FTB (Figure 1; Somoza & Zaffarana, 2008), leading to initial contraction in the area (Ronda et al., 2019). This first Andean contractional stage would have finished after 80 Ma, when a switch from cooling to stagnation in time–temperature paths is shown by most thermal models (Figures 5 and 7).

The data set and thermal models of this work record a cooling phase between 120 and 80 Ma in positively inverted structures of the SPA. During the early stages of Andean shortening and basin inversion, the eastern rim of the orogen could have acted as an intraplate contractional belt as depicted in the proposed evolution of the study area in Figure 8c. This intraplate contractional setting would have been similar to the present San Bernardo FTB and Deseado Massif. This agrees with the analog modeling results of the Austral basin, indicating that early compression in the Patagonian Andes was focused on the inversion of preexisting extensional structures within intraplate systems (Likerman et al., 2013).

5.2. Oligocene-Miocene Cooling: A Record of Progressing Contraction

There is a consensus that the Miocene contraction phase was the consequence of a twofold increase in convergence rates between the Farallon and South American plates after 28–25 Ma (Pardo-Casas & Molnar, 1987; Somoza & Ghidella, 2012). Miocene contraction has been considered the main cause of tectonic crustal shortening, thickening and subsequent surface uplift of the SPA, which favored the deposition of the Santa Cruz Fm. molasse (Encinas et al., 2019; Flint et al., 1994; Lagabrielle et al., 2004; Ramos, 1989; Ramos & Ghiglione, 2008; Ronda et al., 2019). The onset of a rain shadow at ∼14 Ma supports Miocene orogenic growth (Blisniuk et al., 2005). Contractional deformation is recorded in the FTB between 18 and 10 Ma by an angular unconformity between the Miocene Santa Cruz Fm. and Belgrano basalt flows and dikes (10.10 ± 0.32 Ma; Gorring et al., 1997) in the Sierra de Uñas area (Figure 3; Ramos, 1989; Ronda et al., 2019) and in the Meseta Lago Buenos Aires area (Figure 2; Guivel et al., 2006). In the Cosmelli basin (Figure 2) 23-19 Ma sedimentary rocks (Encinas et al., 2019) have also been affected by contraction (Flint et al., 1994).

The ZHe and AFT cooling ages obtained in this study indicate Oligocene–early Miocene cooling coeval with documented contraction across the orogen and are interpreted as a result of thrust-related rock uplift and surface erosion (Figure 8). It is important to note that AFT and ZHe cooling ages are up to 100 Myr younger in the hinterland west of 72.2°W, suggesting that the magnitude of exhumation was at least 5 times larger than east of 72.2°W (Figure 4). Samples from the basement domain (EX1 to EX3, TOR2 to TOR8) crossed the ZHe partial retention zone between 27.9 ± 4.4 Ma and 14.7 ± 2.5 Ma (Figures 2 and 4, Text S2 in Supporting Information S1). Thermal modeling suggests that cooling took place at 7°C/Ma to 2°C/Ma after 30 Ma in hinterland areas (Figure 5). In the Cosmelli basin area, the ZHe results and thermal modeling of reset sample FUR1 suggest Oligocene–Miocene heating followed by cooling since 10 Ma. Toward the east, Oligocene–early Miocene cooling is mainly recorded in AFT ages, while thermal modeling of samples JK1 or FRO1 indicates that cooling restarted later than in the western models, after 20 Ma at average rates of 4°C/Ma (Figures 2–5).

The link between Miocene shortening and cooling agrees with the proposal of Thomson et al. (2001) regarding the migration of the locus of denudation toward the east in response to propagating deformation. Based on the modeling of ZHe-AFT- AHe data, Stevens-Goddard and Fosdick (2019) suggested a northward propagation (from 54 to 47°S) of cooling and rock uplift in response to the erosion of a crustal-welt caused by the migration and collision of the Chile ridge between 20 and 5 Ma. The datasets presented in this study point to a large east–west variability rather than a northward decrease in cooling ages between 48 and 46.5°S (Figures 2 and 4). New Cretaceous ZHe ages obtained toward the foreland (Figures 2–4) are not in agreement with the onset of the cooling trend, partially based on ZHe data modeled by Stevens-Goddard and Fosdick (2019) that would predict Cenozoic ZHe ages for the studied area. Finally, thermal models obtained from foreland samples (Figure 5) show that Cenozoic enhanced cooling would have started prior to 20 Ma, in contrast to the 10 to 7.5 Ma onset of cooling modeled by these authors.

Recently Andrić-Tomašević et al. (2021) tested different exhumational scenarios to reproduce a U-shaped cooling age pattern, partially similar to the trend described in this study (Figure 4). U-shaped cooling age profiles have been associated with the activity of crustal ramps in fold-and-thrust belts (e.g., Coutand et al., 2014; Lock & Willett, 2008; McQuarrie & Ehlers, 2017). Andrić-Tomašević et al. (2021) found that imposing a parabolic exhumation pattern across the orogen at the latitude of study after 15 Ma could reproduce observed thermochronological ages and related such exhumation to the activity of a hypothetical crustal wedge. Such a crustal-wedge structure has been proposed for the area (Ramos, 1989; Ronda et al., 2019, Figures 3 and 5), whose activity could be accountable for the observed cooling-age pattern of this study, in agreement with Andrić-Tomašević et al. (2021). However, Cenozoic contractional activity along such a structure may be earlier than 15 Ma, even as old as 30 Ma in our proposal (Figure 8), as suggested by Oligocene cooling registered in hinterland models such as TOR8 and EX2, related to contractional deformation (Figures 2 and 5).

5.3. Influence of the Patagonian Asthenospheric Window and the Onset of Glaciations in the Thermochronological Record

Among the main effects attributed to the opening of the Miocene PAW is an increase in heat flow and surface uplift (Ávila & Dávila, 2018, 2020; Dávila et al., 2018; Guillaume et al., 2013) that induced changes in regional surface drainage patterns (Guillaume et al., 2009). The hypothesis that the Neogene PAW has heated the upper crust has been proposed by several studies, although the timing and impact assigned to it vary. Inverse thermal modeling of the Cerro Barrancos data indicated upper crustal heating by 50°C–100°C linked to heating processes that preceded Chile ridge collision by 5–10 Myr (Guillaume et al., 2013; Haschke et al., 2006). In contrast, Christeleit et al. (2017) modeled the thermal field response to Chile ridge subduction and concluded that a larger wavelength heating of up to 50°C at 5 km depth in the overriding plate is plausible, rather than a heating peak at 5 Ma. Ridge subduction 3D geodynamic models of Groome and Thorkelson (2009) show that heating of the overriding plate at 5 km depth and 250 km away from the trench (similar to Cerro Barranco's distance) would not have surpassed 150°C. With a similar modeling approach, but a larger number of iterations to those of Guillaume et al. (2013), Georgieva et al. (2019) remodeled the Cerro Barrancos data set and obtained only cooling thermal histories, suggesting that a heating phase is unlikely.

Our modeling results of Cerro Barrancos data, which include a longer thermal history due to the inclusion of ZHe data, show a two cooling steps model without any noticeable heating phase after 20 Ma, nor before, during, or after the collision of the Chile ridge (Figure 7). Neither the ZHe-AFT age distribution (Figures 2–4) nor our thermal modeling results (Figures 5–7) show evidence of regional resetting by a heating phase during the past 10 Myr. The thermochronological data and thermal models (Figures 2, 4 and 5) also show no record of Eocene reheating related to the proposed Eocene Alluk-Farallón asthenospheric window (Ramos & Kay, 1992), rebutting the hypothesis that asthenospheric windows had a thermal effect in the upper crust. Nevertheless, recent heat-flow measurements on deep boreholes suggest that Patagonia has been heated by the asthenospheric window (Ávila & Dávila, 2018, 2020). We argue that the opening of the PAW during the past 5 Ma at the latitude of study may not have happened early enough to have an impact on the analyzed thermochronometers due to its annealing kinetics.

The SPA record glaciations since the latest Miocene at 7 Ma (Figure 8; Mercer & Sutter, 1982; Lagabrielle et al., 2010, and references therein). Preserved landforms comprise cirques and glacial lineations linked to alpine-type glaciers, and depositional landforms such as moraine systems developed east of the study area associated with larger outlet glaciers (Coronato et al., 2004; Glasser et al., 2008). The local Last Glacial Maximum was recorded between 28 and 20 Ka and covered most of the study area (Davies et al., 2020).

The compiled thermochronological datasets and thermal models analyzed in this work agree with the onset of Patagonian glaciations as the main drivers of Miocene to recent rock cooling and exhumation (Andrić-Tomašević et al., 2021; Christeleit et al., 2017; Georgieva et al., 2016; Guillaume et al., 2013; Haschke et al., 2006; Thomson et al., 2010; Willett et al., 2020). However, cooling and exhumation would have not been homogeneous across the orogen according to our findings. Available ZHe and AFT ages as well as thermal models, show a sudden decrease toward younger cooling ages (Figure 3a and 3b) and a twofold increase in cooling rates after 9 Ma (Figure 5) west of 72.2°W. Even though glaciers most likely covered the area east of 72.2°W during the Pleistocene and Pliocene (Coronato et al., 2004; Glasser et al., 2008), ZHe and AFT ages <7 Ma are scarce (Figures 2 and 3), and thermal models do not record accelerated cooling at the times of the Patagonian glaciations (Figure 5) east of this longitude. A possible explanation for this, considering that both areas were affected by the Patagonian glaciations, is that the hinterland experienced higher glacial erosion and exhumation than the foreland during the past 7 Ma, leading to younger cooling ages. This is supported by the record of recent landforms that show that west of 72°W, erosional glacial landforms prevail, while east of 72°W, depositional landforms dominate (Glasser et al., 2008). In addition, higher glacial exhumation toward the hinterland may have been caused by dynamic topography (Guillaume et al., 2009) and/or out-of-sequence thrusting (Ronda et al., 2019; Thomson et al., 2001).

6. Conclusions

New and published thermochronological data and their time–temperature modeling suggest the following:

1. Andean contraction began in this segment sometime between ~120 Ma and ~80 Ma. Shortening produced the inversion of Jurassic extensional structures, promoting cooling at the eastern margin of the orogen in a broken foreland setting.
2. The second deformational phase propagated eastwards across the orogen between 30 and 10 Ma, accompanied by cooling and exhumation in response to tectonic crustal thickening and surface uplift.
3. During the past 7 Ma, no heating due to the opening of an asthenospheric window was recorded. Patagonian glaciations most likely promoted accelerated cooling and exhumation in the hinterland.

Data Availability Statement

All the datasets generated for this work are available in this publication under the form of tables or in the accompanying Supporting Information S1 documents. In addition all datasets are available at the Geochron.org repository at: http://www.geochron.org/dataset/html/geochron_dataset_2022_08_31_32Tda.

Acknowledgments

This work was funded by projects CONICET PIP 11220200100307CO, UBACYT GC 20020190100382BA, PICT-2020-SERIEA-03277 and MINCYT-BMBF AL/17/02 to MG; a doctoral scholarship granted to GR by CONICET Argentina; and an Emerging Leaders in the Americas Program grant provided by Global Affairs Canada to IC for GR. ZHe dating was funded by the U-Th/He laboratory at Dalhousie University. The authors wish to recognize the use of La.Te. Andes - Salta dating facilities and the kind attention given by its staff. Centro de Investigaciones Geológicas La Plata, and Dr. Eugenio Aragón, INGEIS (UBA/CONICET) and the Departamento de Ciencias Geológicas (FCEyN-UBA) are acknowledged for providing access to their facilities. Essential support during field-work in Argentina was provided by the staff at Parque Nacional Perito Moreno; and the Sar family from Lago Posadas. The authors thank Benjamin Guillaume and Cécile Gautheron for providing the zircons from Cerro Barrancos. Kerry Gallagher provided helpful advice for thermal modeling. This work was highly enriched by the thoughtful comments and suggestions of the editor Mauricio Parra, and reviewers Viktoria Georgieva and Federico Dávila. The authors wish to dedicate this article to Dr. Víctor A. Ramos, pioneer tectonist of the Patagonian Andes. This is contribution R-415 of the Instituto de Estudios Andinos "Don Pablo Groeber" (UBA-CONICET).

References

Andrić-Tomašević, N., Falkowski, S., Georgieva, V., Glotzbach, C., Strecker, M. R., & Ehlers, T. A. (2021). Quantifying tectonic and glacial controls on topography in the Patagonian Andes (46.5°S) from integrated thermochronometry and thermokinematic modeling. *Journal of Geophysical Research: Earth Surface*, *126*(8). https://doi.org/10.1029/2020JF005993

Aramendía, I., Ramos, M. E., Geuna, S., Cuitiño, J. I., & Ghiglione, M. C. (2018). A multidisciplinary study of the lower cretaceous marine to continental transition in the northern Austral-Magallanes basin and its geodynamic significance. *Journal of South American Earth Sciences*, *86*, 54–69. https://doi.org/10.1016/j.jsames.2018.06.010

Ault, A. K., Gautheron, C., & King, G. E. (2019). Innovations in (U–Th)/He, fission track, and trapped charge thermochronometry with applications to earthquakes, weathering, surface-mantle connections, and the growth and decay of mountains. *Tectonics*, *38*(11), 3705–3739. https://doi.org/10.1029/2018TC005312

Blisniuk, P. M., Stern, L. A., Chamberlain, C. P., Idleman, B., & Zeitler, P. K. (2005). Climatic and ecologic changes during Miocene surface uplift in the southern Patagonian Andes. *Earth and Planetary Science Letters*, *230*(1–2), 125–142. https://doi.org/10.1016/j.epsl.2004.11.015

Breitsprecher, K., & Thorkelson, D. J. (2009). Neogene kinematic history of Nazca-Antarctic-Phoenix slab windows beneath Patagonia and the Antarctic Peninsula. *Tectonophysics*, *464*(1–4), 10–20. https://doi.org/10.1016/j.tecto.2008.02.013

Calderón, M., Fildani, A., Hervé, F., Fanning, C. M., Weislogel, A., & Cordani, U. (2007). Late Jurassic bimodal magmatism in the northern sea-floor remnant of the Rocas Verdes basin, southern Patagonian Andes. *Journal of the Geological Society*, *164*(5), 1011–1022. https://doi.org/10.1144/0016-76492006-102

Cande, S. C., & Leslie, R. B. (1986). Late cenozoic tectonics of the southern Chile trench. *Journal of Geophysical Research*, *91*(B1), 471–496. https://doi.org/10.1029/jb091ib01p00471

Cembrano, J., Hervé, F., & Lavenu, A. (1996). The Liquiñe Ofqui fault zone: A long-lived intra-arc fault system in southern Chile. *Tectonophysics*, *259*(1–3), 55–66. https://doi.org/10.1016/0040-1951(95)00066-6

Christeleit, E. C., Brandon, M. T., & Shuster, D. L. (2017). Miocene development of alpine glacial relief in the Patagonian Andes, as revealed by low-temperature thermochronometry. *Earth and Planetary Science Letters*, *460*, 152–163. https://doi.org/10.1016/j.epsl.2016.12.019

Colwyn, D. A., Brandon, M. T., Hren, M. T., Hourigan, J., Pacini, A., Cosgrove, M. G., et al. (2019). Growth and steady state of the Patagonian Andes. *American Journal of Science*, *319*(6), 431–472. https://doi.org/10.2475/06.2019.01

Coronato, A., Martínez, O., & Rabassa, J. (2004). Glaciations in Argentine Patagonia, southern south America. In *Developments in quaternary sciences* (Vol. 2, pp. 49–67). Elsevier.

Coutand, I., Whipp, D. M., Jr., Grujic, D., Bernet, M., Fellin, M. G., Bookhagen, B., et al. (2014). Geometry and kinematics of the main Himalayan thrust and Neogene crustal exhumation in the Bhutanese Himalaya derived from inversion of multithermochronologic data. *Journal of Geophysical Research: Solid Earth*, *119*(2), 1446–1481. https://doi.org/10.1002/2013JB010891

Cristallini, E., Hernández, R., Balciunas, D., Nigro, J., Dellmans, M., & Costilla, M. (2019). Andino 3D: Structural modeling software (Version 2.0.0.6) [Software]. CONICETLATE. https://www.andino3d.com.ar/descargas

Cuitiño, J. I., Santos, R. V., Alonso Muruaga, P. J., & Scasso, R. A. (2015). Estratigrafía de Sr y evolución sedimentaria de los depósitos marinos del Mioceno temprano en el antepaís del norte de la Cuenca Austral (O Magallanes), Argentina. *Andean Geology*, *42*(3), 364–385. https://doi.org/10.5027/andgeoV42n3-a05

Davies, B. J., Darvill, C. M., Lovell, H., Bendle, J. M., Dowdeswell, J. A., Fabel, D., et al. (2020). The evolution of the Patagonian Ice Sheet from 35 ka to the present day (PATICE). *Earth-Science Reviews*, *204*, 103152. https://doi.org/10.1016/j.earscirev.2020.103152

De La Cruz, R., Welkner, D., Suárez, M., & Quiroz, D. (2004). Geología del Área Oriental de las Hojas Cochrane y Villa O'Higgins, Región Aisén del General Carlos Ibáñez del Campo. Servicio Nacional de Geología y Minería, Carta Geológica de Chile. *Serie Geología Básica*, *85*, 57. Map scale 1:250, 000.

DeMets, C., Gordon, R. G., & Argus, D. F. (2010). Geologically current plate motions. *Geophysical Journal International*, *181*(1), 1–80. https://doi.org/10.1111/j.1365-246x.2009.04491.x

Dávila, F. M., & Carter, A. (2013). Exhumation history of the Andean broken foreland revisited. *Geology*, *41*(4), 443–446. https://doi.org/10.1130/g33960.1

Dávila, F. M., Lithgow-Bertelloni, C., Martina, F., Ávila, P., Nobile, J., Collo, G., et al. (2018). Mantle influence on Andean and pre-Andean topography (pp. 363–385).

Encinas, A., Folguera, A., Riffo, R., Molina, P., Fernández Paz, L., Litvak, V. D., et al. (2019). Cenozoic basin evolution of the central Patagonian Andes: Evidence from geochronology, stratigraphy, and geochemistry. *Geoscience Frontiers*, *10*(3), 1139–1165. https://doi.org/10.1016/j.gsf.2018.07.004

Espinoza, F., Morata, D., Pelleter, E., Maury, R. C., Suárez, M., Lagabrielle, Y., et al. (2005). Petrogenesis of the Eocene and Mio-Pliocene alkaline basaltic magmatism in Meseta Chile Chico, southern Patagonia, Chile: Evidence for the participation of two slab windows. *Lithos*, *82*(3–4), 315–343. https://doi.org/10.1016/j.lithos.2004.09.024

Farley, K. A. (2000). Helium diffusion from apatite: General behavior as illustrated by Durango fluorapatite. *Journal of Geophysical Research*, *105*(B2), 2903–2914. https://doi.org/10.1029/1999jb900348

Fernández, M. L., Mazzoli, S., Zattin, M., Savignano, E., Genge, M. C., Tavani, S., et al. (2020). Structural controls on jurassic gold mineralization, and cretaceous-tertiary exhumation in the foreland of the southern Patagonian Andes: New constraints from La Paloma area, Deseado Massif, Argentina. *Tectonophysics*, *775*, 228302. https://doi.org/10.1016/j.tecto.2019.228302

Flint, S. S., Prior, D. J., Agar, S. M., & Turner, P. (1994). Stratigraphic and structural evolution of the Tertiary Cosmelli Basin and its relationship to the Chile triple junction. *Journal of the Geological Society*, *151*(2), 251–268. https://doi.org/10.1144/gsjgs.151.2.0251

Fosdick, J. C., Grove, M., Hourigan, J. K., & Calderon, M. (2013). Retroarc deformation and exhumation near the end of the Andes, southern Patagonia. *Earth and Planetary Science Letters*, *361*, 504–517. https://doi.org/10.1016/j.epsl.2012.12.007

Gallagher, K. (2012). Transdimensional inverse thermal history modeling for quantitative thermochronology. *Journal of Geophysical Research*, *117*(B2). https://doi.org/10.1029/2011JB008825

Georgieva, V., Gallagher, K., Sobczyk, A., Sobel, E. R., Schildgen, T. F., Ehlers, T. A., & Strecker, M. R. (2019). Effects of slab-window, alkaline volcanism, and glaciation on thermochronometer cooling histories, Patagonian Andes. *Earth and Planetary Science Letters*, *511*, 164–176. https://doi.org/10.1016/j.epsl.2019.01.030

Georgieva, V., Melnick, D., Schildgen, T. F., Ehlers, T. A., Lagabrielle, Y., Enkelmann, E., & Strecker, M. R. (2016). Tectonic control on rock uplift, exhumation, and topography above an oceanic ridge collision: Southern Patagonian Andes (47°S), Chile. *Tectonics*, *35*(6), 1317–1341. https://doi.org/10.1002/2016TC004120

Ghiglione, M. C., Naipauer, M., Sue, C., Barberón, V., Valencia, V., Aguirre-Urreta, B., & Ramos, V. A. (2015). U-Pb zircon ages from the northern Austral basin and their correlation with the Early Cretaceous exhumation and volcanism of Patagonia. *Cretaceous Research*, *55*, 116–128. https://doi.org/10.1016/j.cretres.2015.02.006

Ghiglione, M. C., Ramos, V. A., Cuitiño, J., & Barberón, V. (2016). Growth of the southern Patagonian Andes (46–53 S) and their relation to subduction processes. In *Growth of the southern Andes* (pp. 201–240). Springer.

Ghiglione, M. C., Ronda, G., Suárez, R. J., Aramendía, I., Barberón, V., Ramos, M. E., et al. (2019). *Structure and tectonic evolution of the South Patagonian fold and thrust belt: Coupling between subduction dynamics, climate and tectonic deformation, Andean Tectonics*. Elsevier Inc. https://doi.org/10.1016/b978-0-12-816009-1.00024-1

Giacosa, R., Zubia, M., Sánchez, M., & Allard, J. (2010). Meso-cenozoic tectonics of the southern Patagonian foreland: Structural evolution and implications for Au–Ag veins in the eastern Deseado region (Santa Cruz, Argentina). *Journal of South American Earth Sciences*, *30*(3–4), 134–150. https://doi.org/10.1016/j.jsames.2010.09.002

Gianni, G. M., Navarrete, C., Liendo, I., Díaz, M., Giménez, M. E., Encinas, A., & Folguera, A. (2018). Cretaceous intraplate contraction in southern Patagonia: A far-field response to changing subduction dynamics? *Tectonics*, *37*(9), 2915–2937. https://doi.org/10.1029/2018TC005173

Gianni, G., Navarrete, C., Orts, D., Tobal, J., Folguera, A., & Giménez, M. (2015). Patagonian broken foreland and related synorogenic rifting: The origin of the chubut group basin. *Tectonophysics*, *649*, 81–99. https://doi.org/10.1016/j.tecto.2015.03.006

Glasser, N. F., Jansson, K. N., Harrison, S., & Kleman, J. (2008). The glacial geomorphology and Pleistocene history of South America between 38 S and 56 S. *Quaternary Science Reviews*, *27*(3–4), 365–390. https://doi.org/10.1016/j.quascirev.2007.11.011

Gorring, M. L., Kay, S. M., Zeitler, P. K., Ramos, V. A., Rubiolo, D., Fernandez, M. I., & Panza, J. L. (1997). Neogene Patagonian plateau lavas: Continental magmas associated with ridge collision at the Chile Triple Junction. *Tectonics*, *16*, 1–17. https://doi.org/10.1029/96TC03368

Groome, W. G., & Thorkelson, D. J. (2009). The three-dimensional thermo-mechanical signature of ridge subduction and slab window migration. *Tectonophysics*, *464*(1–4), 70–83.

Guenthner, W. R., Reiners, P. W., Ketcham, R. A., Nasdala, L., & Giester, G. (2013). Helium diffusion in natural zircon: Radiation damage, anisotropy, and the interpretation of zircon (U-TH)/He thermochronology. *American Journal of Science*, *313*(3), 145–198. https://doi.org/10.2475/03.2013.01

Guillaume, B., Gautheron, C., Simon-Labric, T., Martinod, J., Roddaz, M., & Douville, E. (2013). Dynamic topography control on Patagonian relief evolution as inferred from low temperature thermochronology. *Earth and Planetary Science Letters*, *364*, 157–167. https://doi.org/10.1016/j.epsl.2012.12.036

Guillaume, B., Martinod, J., Husson, L., Roddaz, M., & Riquelme, R. (2009). Neogene uplift of central eastern Patagonia: Dynamic response to active spreading ridge subduction? *Tectonics*, *28*(2), 1–19. https://doi.org/10.1029/2008TC002324

Guivel, C., Morata, D., Pelleter, E., Espinoza, F., Maury, R. C., Lagabrielle, Y., et al. (2006). Miocene to Late Quaternary Patagonian basalts (46–47 S): Geochronometric and geochemical evidence for slab tearing due to active spreading ridge subduction. *Journal of Volcanology and Geothermal Research*, *149*(3–4), 346–370. https://doi.org/10.1016/j.jvolgeores.2005.09.002

Haschke, M., Sobel, E. R., Blisniuk, P., Strecker, M. R., & Warkus, F. (2006). Continental response to active ridge subduction. *Geophysical Research Letters*, *33*(15), 1–5. https://doi.org/10.1029/2006GL025972

Herman, F., Seward, D., Valla, P. G., Carter, A., Kohn, B., Willett, S. D., & Ehlers, T. A. (2013). Worldwide acceleration of mountain erosion under a cooling climate. *Nature*, *504*(7480), 423–426. https://doi.org/10.1038/nature12877

Hernandez-Moreno, C., Speranza, F., & Di Chiara, A. (2014). Understanding kinematics of intra-arc transcurrent deformation: Paleomagnetic evidence from the Liquiñe-Ofqui fault zone (Chile, 38–41°S). *Tectonics*, *33*(10), 1964–1988. https://doi.org/10.1002/2014TC003622

Hervé, F., Pankhurst, R. J., Fanning, C. M., Calderón, M., & Yaxley, G. M. (2007). the South Patagonian batholith: 150 my of granite magmatism on a plate margin. *Lithos*, *97*(3–4), 373–394. https://doi.org/10.1016/j.lithos.2007.01.007

Ketcham, R. A. (2005). Forward and inverse modeling of low-temperature thermochronometry data. *Reviews in Mineralogy and Geochemistry*, *58*(1), 275–314. https://doi.org/10.2138/rmg.2005.58.11

Ketcham, R. A., Carter, A., Donelick, R. A., Barbarand, J., & Hurford, A. J. (2007). Improved modeling of fission-track annealing in apatite. *American Mineralogist*, *92*(5–6), 799–810. https://doi.org/10.2138/am.2007.2281

Lagabrielle, Y., Scalabrino, B., Suarez, M., & Ritz, J. F. (2010). Mio-Pliocene glaciations of Central Patagonia: New evidence and tectonic implications. *Andean Geology*, *37*(2), 276–299.

Lagabrielle, Y., Suárez, M., Rossello, E. A., Hérail, G., Martinod, J., Régnier, M., & de la Cruz, R. (2004). Neogene to quaternary tectonic evolution of the Patagonian Andes at the latitude of the Chile triple junction. *Tectonophysics*, *385*(1–4), 211–241. https://doi.org/10.1016/j.tecto.2004.04.023

Likerman, J., Burlando, J. F., Cristallini, E. O., & Ghiglione, M. C. (2013). Along-strike structural variations in the southern Patagonian Andes: Insights from physical modeling. *Tectonophysics*, *590*, 106–120. https://doi.org/10.1016/j.tecto.2013.01.018

Lock, J., & Willett, S. (2008). Low-temperature thermochronometric ages in fold-and-thrust belts. *Tectonophysics*, *456*(3–4), 147–162. https://doi.org/10.1016/j.tecto.2008.03.007

McQuarrie, N., & Ehlers, T. A. (2017). Techniques for understanding fold-and-thrust belt kinematics and thermal evolution.

Mercer, J. H., & Sutter, J. F. (1982). Late Miocene—Earliest Pliocene glaciation in southern Argentina: Implications for global ice-sheet history. *Palaeogeography, Palaeoclimatology, Palaeoecology*, *38*(3–4), 185–206. https://doi.org/10.1016/0031-0182(82)90003-7

Ottone, E. G., & Aguirre-Urreta, M. B. (2000). Nota Paleontológica. Palinomorfos cretácicos de la Formación Springhill en Estancia El Salitral, Patagonia austral, Argentina. *Ameghiniana*, *37*(3), 379–382.

Pankhurst, R. J., Riley, T. R., Fanning, C. M., & Kelley, S. P. (2000). Episodic silicic volcanism in Patagonia and the Antarctic Peninsula: Chronology of magmatism associated with the break-up of Gondwana. *Journal of Petrology*, *41*(5), 605–625. https://doi.org/10.1093/petrology/41.5.605

Pankhurst, R. J., Weaver, S. D., Hervé, F., & Larrondo, P. (1999). Mesozoic-cenozoic evolution of the North Patagonian batholith in Aysen, southern Chile. *Journal of the Geological Society*, *156*(4), 673–694. https://doi.org/10.1144/gsjgs.156.4.0673

Pardo-Casas, F., & Molnar, P. (1987). Relative motion of the Nazca (Farallon) and south American plates since late cretaceous time. *Tectonics*, *6*(3), 233–248. https://doi.org/10.1029/tc006i003p00233

Ramos, V. A. (1989). Andean foothills structures in Northern Magallanes basin, Argentina. *The American Association of Petroleum Geologists Bulletin*, *73*, 887–903.

Ramos, V. A., & Ghiglione, M. C. (2008). Tectonic evolution of the Patagonian Andes. *Developments in Quaternary Science*, *11*, 57–71.

Ramos, V. A., & Kay, S. M. (1992). Southern Patagonian plateau basalts and deformation: Backarc testimony of ridge collisions. *Tectonophysics*, *205*(1–3), 261–282. https://doi.org/10.1016/0040-1951(92)90430-E

Ronda, G., Ghiglione, M., Barberón, V., Coutand, I., & Tobal, J. (2019). Mesozoic – Cenozoic evolution of the southern Patagonian Andes fold and thrust belt (47°–48°S): Influence of the Rocas Verdes basin inversion and onset of Patagonian glaciations. *Tectonophysics*, *765*, 83–101. https://doi.org/10.1016/j.tecto.2019.05.009

Schwanghart, W., & Scherler, D. (2014). Short communication: TopoToolbox 2 - MATLAB-based software for topographic analysis and modeling in Earth surface sciences. *Earth Surface Dynamics*, *2*, 1–7. https://doi.org/10.5194/esurf-2-1-2014

Somoza, R., & Ghidella, M. E. (2012). Late Cretaceous to recent plate motions in Western South America revisited. *Earth and Planetary Science Letters*, *331–332*, 152–163. https://doi.org/10.1016/j.epsl.2012.03.003

Somoza, R., & Zaffarana, C. B. (2008). Mid-Cretaceous polar standstill of South America, motion of the Atlantic hotspots and the birth of the Andean cordillera. *Earth and Planetary Science Letters*, *271*(1–4), 267–277. https://doi.org/10.1016/j.epsl.2008.04.004

Stevens Goddard, A., Fosdick, J. C., & Martinod, J. (2019). Multichronometer thermochronologic modeling of migrating spreading ridge subduction in southern Patagonia. *Geology*, *47*(10), e483. https://doi.org/10.1130/G46629C.1

Sánchez, A. (2011). *Génesis del plutonismo cenozoico en la Patagonia extra-andina al sur del punto triple*. Tesis de doctorado de la Universidad de Chile.

Thomson, S. N., Brandon, M. T., Tomkin, J. H., Reiners, P. W., Vásquez, C., & Wilson, N. J. (2010). Glaciation as a destructive and constructive control on mountain building. *Nature*, *467*(7313), 313–317. https://doi.org/10.1038/nature09365

Thomson, S. N., Hervé, F., & Stökhert, B. (2001). Mesozoic-Cenozoic denudation history of the Patagonian Andes (Southern Chile) and its correlation to different subduction processes. *Tectonics*, *20*(5), 693–711. https://doi.org/10.1029/2001TC900013

Welkner, D., Godoy, E., & Bernhardt, H. J. (2002). Peralkaline rocks in the late cretaceous del Salto Pluton, eastern Patagonian Andes, Aisén, Chile (47°35'S). *Revista Geologica de Chile*, *29*(1). https://doi.org/10.4067/S0716-02082002000100001

Willett, C. D., Ma, K. F., Brandon, M. T., Hourigan, J. K., Christeleit, E. C., & Shuster, D. L. (2020). Transient glacial incision in the Patagonian Andes from ~6 Ma to present. *Science Advances*, *6*(7), 1–10. https://doi.org/10.1126/sciadv.aay1641

Ávila, P., & Dávila, F. M. (2018). Heat flow and lithospheric thickness analysis in the Patagonian asthenospheric windows, southern South America. *Tectonophysics*, *747*, 99–107. https://doi.org/10.1016/j.tecto.2018.10.006

Ávila, P., & Dávila, F. M. (2020). Lithospheric thinning and dynamic uplift effects during slab window formation, southern Patagonia (45°–55°S). *Journal of Geodynamics*, *133*, 101689. https://doi.org/10.1016/j.jog.2019.101689